DEEP CCD PHOTOMETRY IN THE GLOBULAR CLUSTER M10

by

DANIEL JOSEPH COLMAN HURLEY

B.Sc., University of New Brunswick, 1986

A THESIS SUBMITTED IN PARTIAL FULFILLMENT OF
THE REQUIREMENTS FOR THE DEGREE OF
MASTER OF SCIENCE

in

THE FACULTY OF GRADUATE STUDIES

Department of Geophysics and Astronomy

We accept this thesis as conforming
to the required standard

THE UNIVERSITY OF BRITISH COLUMBIA

March 1989

Department of Geophysics and Astronomy

The University of British Columbia
Vancouver, Canada

Date 25 April 1989

Abstract

CCD observations of the galactic globular cluster NGC 6254 (M10), obtained at the Canada-France-Hawaii 3.6 m telescope, have been reduced and analysed. A color-magnitude diagram of the cluster which extends below $V = 21$ is presented. The basic observational parameters of distance modulus, reddening and metallicity are derived. The latter two values are in excellent agreement with results in the literature. The distance modulus is $0^{m}_{\cdot}3$ larger than previous estimates. Possible implications of this discrepancy are considered. The morphology of the color-magnitude diagram, in particular the very blue horizontal branch which is observed down to the turnoff luminosity, is discussed in terms of the "second parameter" problem. The age of M10 is estimated to be 17 ± 1 Gyr, through use of Vandenberg and Bell's (1985) isochrones. A comparison to the color-magnitude diagram of NGC 288 produced by Bolte (1989b) to that of M10 indicates that these two clusters are coeval. Luminosity functions are generated for the three fields observed in M10 and translated into mass functions. By comparing those mass functions to multimass King models a global mass function exponent of $x_{global} = 0.5 \pm 0.5$ is found. The mass function is quite uniform in slope in the range $0.5-0.8\,M_{\odot}$. No firm evidence for mass segregation was seen, but these data are not particularly sensitive to such effects.

Contents

List of Tables

List of Figures

Acknowledgements

I would like to express my thanks to Dr. Harvey Richer and Dr. Gregory Fahlman who were co-supervisors of this project, obtained data, provided financial support and generally kept things on track. I am indebted to Dr. René Racine for permission to reproduce Plate 2 from Harris, Racine and de Roux (1976) which appears as Figure 3.1 in this work. I am also indebted to Dr. James Nemec who assisted in obtaining the RCA2 data. I am grateful to my fellow graduate students, and Dr. Jaymie Matthews, for providing fine targets for my ever nasty sense of humor and for some reason putting up with me. Nadine Dinshaw and Jaymie were kind enough to help check my dreadful spëlløng and offer stylistic advice. Dr. Gerry Grieve helped keep me hiking and reintroduced me to orienteering. Dr. Jason Auman was always encouraging with his sunny disposition and pleasant chit chat (that's "Drill Sergeant Auman, *Sir!*", to us graduate students).

My longstanding roommate Pam has been a constant source of support, and remarkably tolerant of my moods in the months leading to the completion of this thesis. I must especially thank Tara for, in a really weird kind of way, helping to keep me sane these last few months.

Most importantly I would like to once again express my deepest sympathy to the Kindl family, and to thank them for the establishment of the Enrico Kindl Memorial Fund.

Chapter 1

Introduction

The study of globular clusters, like many other fields in astronomy, has gained immensely from new array-detector technology and access to observing sites which routinely offer sub-arcsecond seeing. The tremendous dynamic range of CCD detectors seems almost uniquely suited to globular cluster research. Before the advent of such detectors, analysis of the crowded centers of globular clusters was restricted to their gross integrated properties. Now, thousands of stars spanning a range of 9–10 magnitudes in luminosity, packed into a field of a few square arcminutes, are available in a single CCD image.

Globular clusters are playing a role of increasing interest in astronomy, due only in part to these recent observational advances. Because globular clusters are very old structures, they are of cosmological importance. The age of the oldest globular cluster, with time added for primordial material to cool and the galactic halo to form, sets a hard lower bound on the age of the Universe. Since all the stars in a globular cluster have very nearly the same age and composition, these clusters provide relatively uncontaminated settings to study stellar evolution. In fact, recent studies (Hesser *et al.* 1987, Richer and Fahlman 1986,1987) have found that the main sequence of a typical globular cluster is often of essentially zero intrinsic width, implying a dispersion in metallicity no greater than a few tenths of a dex.

Globular clusters are also interesting laboratories for the study of stellar dynamics, a field whose roots lie in statistical thermodynamics. Globular clusters contain enough bodies that random motions of stars tend to average out over the cluster.

A binary system illustrates the simplest case in stellar dynamics, the two-body problem, which is unique in that it may be solved analytically. Two- or few-body problems may be integrated directly and are not very relevant to tests of statistical methods. The other extreme of stellar dynamics is a galaxy, where a huge number of stars ($\geq 10^9$) interact with one another and diffuse nonstellar material, all in a usually non-spherical system. Galaxies contain so many stars that direct integration of the orbits of all the bodies involved (stellar *and* nonstellar) would consume a prohibitive amount of time, even on the fastest computing engines foreseeable.

Globular clusters occupy a convenient middle ground in this continuum; few body systems may be directly integrated, and galaxy sized systems suffer complicated effects from awkward initial conditions. If the dynamics of these mid-scale systems can be understood, problems involving larger systems, of greater complexity, and with different symmetries, may be tackled with greater confidence and insight.

In this paper the results of a new study of the globular cluster NGC 6254 (M10) are presented. These include a deep color-magnitude diagram extending to the main sequence, and luminosity and mass functions obtained at different radii within the cluster. The data are used to establish the age of M10 and search for mass segregation among the cluster stars.

Chapter 2

Globular Clusters

A globular cluster is a roughly spherical collection of some $10^4 - 10^6$ stars. These clusters orbit in a halo about the Galaxy. Currently, about 175 globular clusters are known. These clusters probably represent an almost complete inventory of the Galactic globular cluster system, with the exception of those clusters obscured by the Galaxy itself.

The "Crown Jewels" of the globular cluster system, from the Earth's vantage point, are 47 Tuc and ω Cen, both in the Southern hemisphere, they are both naked eye objects, under 10 kpc distant. 47 Tuc is one of the most metal-rich globular clusters, with $[\mathrm{Fe/H}] = -0.75$. ω Cen is of intermediate metallicity, but contains in excess of 160 variable stars, both RR Lyraes and Cepheids. In the Northern Hemisphere, the brightest globular cluster is the high galactic latitude (virtually zero reddening) globular cluster M13, which is of intermediate metallicity. Two other important Northern globular clusters are M15 and M92, both notable for their low metallicity. The properties of several globular clusters are discussed and compared to those of M10 in §2.3. Unless otherwise noted properties of specific globular clusters are taken from Webbink (1985).

Globular clusters, though generally individually homogeneous, span a wide range of chemical properties as a family. The most metal-poor clusters are under abundant by a factor of 100 compared to the Sun; the richest display up to a third of the solar abundance. This wide variation provides an excellent means of testing the effects of varying metal abundances in stellar evolution models.

The importance of globular clusters was first recognized as a probe of galactic structure by Shapley (1918). From our position within the halo of globular clusters, assumed to be symmetric about the galactic center, our position within the Galaxy was inferred. Also, the extent of the halo better defines the overall size of our Galaxy (Arp 1965).

Globular clusters consist of Population II stars. The stellar population concept was introduced by Baade (1944a,b). Baade recognized that the brightest stars in elliptical galaxies and the bulges of spiral galaxies were red in color, similar to the brightest stars in globular clusters. However the brightest stars in the disks of spiral galaxies were blue. Stars associated with the former group became known as Population I stars, and those associated with the latter Population II. Eventually an inverse relation between metal abundance and age was inferred. Globular clusters occupy a key role in the understanding of the chemical and physical evolution of our, and other, galaxies.

2.1 Stellar Dynamics in Globular Clusters

Since the pioneering work of Chandrasekhar (1943a, 1943b, 1960) the study of globular cluster dynamics has been an active field. A complete discussion of the topic is far beyond the scope of this work. Many excellent review articles have been written on the subject (Lightman and Shapiro 1978 and Spitzer 1984,1987)

Globular clusters probably condensed from the proto-galactic cloud of material, as the galaxy was forming. The globular clusters may have formed at different times to account for the range of metallicities observed. This metal enhancement may have come from an early population of stars, or may result from cluster self-enrichment, or a combination of both. Once formed, the evolution of a globular cluster is governed by the gravitational interaction of its member stars with each other, with the overall potential of the cluster and with the gravitational field of the galaxy.

There are two relevant time scales concerning globular cluster evolution, the crossing, or dynamical time, t_d, and a relaxation time, t_r. The crossing time is how long a star, moving with typical velocity will take to traverse the cluster. In most cases t_d is under 10^6 years. The relaxation time can be thought of as the time taken for an average star to "forget" about its initial kinematic conditions. The relaxation time is a function of both the age of the cluster and radius; however t_r remains relatively constant at the radius which contains half the mass of the cluster. When the relaxation time is calculated at this half-mass radius, it is denoted as t_{rh}. In systems with large numbers of stars, the relaxation time greatly exceeds the crossing time (specifically,

$t_d/t_{rh} \sim \ln N/N$). The relaxation time is shorter in the core than the less dense outer regions of the cluster, due to the greater frequency of stellar encounters near the center. Over a time scale closer to t_d than t_{rh}, a cluster settles into virial equilibrium and develops a concentrated core with a quasi-Maxwellian velocity distribution. This phenomena has been dubbed "Violent Relaxation" by Lynden-Bell (1967).

A globular cluster which is isolated in space might be expected to assume a perfectly Maxwellian velocity distribution. However, in the galactic neighbourhood there is a slow loss of stars from the cluster caused by stars being captured by the galactic gravitational field.

Since t_{rh} is shorter in the isothermal core than in the cluster as a whole, stars will be depleted preferentially from the core and moved to the cluster halo, and perhaps lost to the cluster. As each star is eliminated from the core, the average binding energy of the remaining stars increases. Therefore, the stars ejected into the halo from the core are increasingly energetic and the halo begins to grow. The core and halo become more structurally distinct; the core shrinks and becomes more tightly bound while the halo expands.

The core will continue to collapse until, with only 1000 or fewer core members remaining, the density stellar is high enough that new types of interactions become important. At very high densities, the probability of forming binaries, or even stars coalescing, becomes very large. Once formed, one or more very massive stars or binaries could, through interactions with the other members of the core, rapidly dissipate the core. Many clusters have high luminosity x-ray sources near their cores, indicating the presence of a binary containing a neutron star.

If a binary forms with binding energy much greater than the kinetic energy of the surrounding stars, it is referred to as a "hard" binary. When a hard binary interacts with another star, it becomes more tightly bound while the other star is ejected at high speed. The binding energy of a single hard binary may well exceed the total energy of the rest of the stars in the isothermal core.

Thus, a globular cluster undergoes three distinct phases of dynamical evolution. After its initial relaxation, most of the cluster's life is spent approaching core collapse. The final stage is post core collapse dispersion of the core and eventual tidal dispersal of the remaining stars.

2.1.1 Mass Segregation

The net result of many binary interactions between cluster members is that the kinetic energy of all the stars will tend toward an average. Eventually stars of higher mass will have systematically lower velocities, and lower mass stars will have, on average, higher velocities. As all the cluster members orbit the gravitational center of the cluster, this implies that light stars will spend more time in the cluster halo, as a higher velocity implies a larger orbital axis. Conversely, heavy stars will congregate near the cluster center. This phenomenon is referred to as mass segregation, or stratification.

Mass segregation should be observable in globular clusters, as higher ratio of high mass to low mass stars toward the cluster center. Care must be taken in the observations; increased crowding of an image near the cluster center, making less massive (fainter) stars more difficult to observe, could mimic the effects of mass segregation.

2.2 King Models

A class of models called King models have been developed (King, 1966a), which describe the surface brightness profiles of observed globular clusters. These models are based on lowered Maxwellian distributions, approximations to the solution of the Fokker-Planck equation. This equation can be used to describe the velocity distribution of stars in a globular cluster. These models have only a single input parameter, the central potential of the cluster. Near the core the densities of King models are similar to the isothermal sphere, but the density falls below the isothermal case to zero at a finite radius identified with the tidal radius.

King models are not physically realistic. Real globular clusters display a range of stellar masses, while King models have only a single stellar mass. Despite this shortcoming, King models do accurately describe the surface brightness profile of a great number of globular clusters. A few globular clusters show a centrally peaked, cusp-like central brightness feature which King models fail to describe. These clusters may be highly evolved. More complex models are often built upon the King models by providing for a range of masses and velocity anisotropy. The classic work in this area is that of Gunn and Griffin (1979).

2.3 M10

M10 is a southern globular cluster, located in the constellation Ophiuchus. M10 is of intermediate metallicity and is very highly reddened. M10 has an extremely blue horizontal branch, as revealed by Arp (1955). Nemec (1975) notes that M10 has a very heavily populated blue horizontal branch, with very few stars on the red horizontal and asymptotic giant branches. Four variable stars have been identified in M10, by Sawyer Hogg (1973) and only one of these may be an RR-Lyrae star.

The definitive early work on M10 was that of Arp (1955). This study produced a color-magnitude diagram extending to 16$^{\rm th}$ magnitude. The very blue horizontal branch was observed down to the plate limit; modern studies reveal that the horizontal branch extends to at least $V = 18$.

Had good metallicity indicators been available at the time, the second parameter problem may have been recognized in the data presented by Arp (1955). This problem concerns the distribution of stars on the horizontal branch, which may depend on some parameter other than metallicity alone. Of the clusters studied by Arp, M3, M5, M13 and M10 are all now identified as intermediate metallicity clusters. Of these four clusters M10 and M13 have very blue horizontal branches, while M3 and M5 have horizontal branches which are well populated on both sides of the RR Lyrae gap.

The most thorough study of M10 based on photographic data was conducted by Harris, Racine and deRoux (1976). (Hereafter Harris, Racine and deRoux (1976) will be referred to as HRdR.) Their work extended the color-magnitude diagram by two magnitudes to $V = 18$. HRdR estimate the reddening to be about $0^{\rm m}\!\!.26\ \pm 0^{\rm m}\!\!.02$, by comparing their color-magnitude diagram to a color-magnitude diagram for M13.

The most recent M10 color-magnitude diagram in the literature is due to Samus and Shugarov (1983). Their photographic observations with a 6 m telescope do reveal stars below the turnoff at $V = 18^{\rm m}\!\!.4$, down to a limit of $19^{\rm m}\!\!.5$. Unfortunately the photometric scatter is very large, $\sim 0^{\rm m}\!\!.3$ in color at the turnoff, and very few horizontal branch stars appear in the color-magnitude diagram. Samus and Shugarov report a large value for the turnoff to horizontal branch magnitude difference, $\Delta V_{HB}^{TO} \approx 3^{\rm m}\!\!.8$ which exceeds the expected value of $3^{\rm m}\!\!.55$ (Buonanno, *et al.* 1989). Samus and Shugarov use the level of the horizontal branch reported by HRdR. However, since the horizontal branch in M10 is very blue, it is difficult to reliably measure any quantities based on the level of the horizontal branch.

Table 2.1 gives published values of several parameters for M10. Note that these data are not determined from this work; rather, the table summerizes the state of knowledge of M10 before this new study was undertaken. Table 2.2 contains the corresponding parameters for a few other well studied clusters for comparison with M10.

property	notes	value	references
Object		NGC 6254	
Name		M10	
α_{1950}		$16^h54^m31^s$	(A)
δ_{1950}		$-04°01.4'$	(A)
b		$+23°$	(A)
$\log\theta_t$	(1)	1.38	(A)
$\log\theta_c$	(2)	−0.15, −0.11	(A,B)
$\log \mathrm{T_r}$	(3)	8.023, 8.18	(A,B)
$\log\rho_o$	(4)	3.765, 3.69	(A,B)
$\mathrm{V_{HB}}$	(5)	14.65	(C)
$B/(B+R)$	(6)	0.94	(D)
$(\mathrm{m}-\mathrm{M})_V$		14.1	(C)
$\mathrm{E}(B-V)$		0.26	(C)
[Fe/H]		−1.51, −1.5, −1.43, −1.60	(A,E,F,G)

Table 2.1: Properties of M10. Notes: (1) Log of tidal radius in arc minutes. (2) Log of core radius in arc minutes. (3) Log of central relaxation time in years. (4) Log of central density in $\mathrm{M_\odot/pc^3}$. (5) Magnitude of horizontal branch. (6) Fraction of non-RR Lyrae horizontal branch population on blue side of RR-Lyrae strip. References: (A) Webbink (1985). (B) Peterson and King (1975). (C) Harris, Racine and deRoux (1976). (D) Zinn (1980). (E) Osborn (1973). (F) Harris and Racine (1979). (G) Zinn and West (1984).

NGC	104	5139	5272	5904	6205	6752	288	6341
Name	47 Tuc	ω Cen	M3	M5	M13			M92
b	−44.9	+15.0	+78.7	+46.9	+40.9	−25.6	-89.4	+34.9
$\log\theta_t$	1.65	1.64	1.59	1.46	1.43	1.49	1.19	1.22
$\log\theta_c$	−0.41	0.42	−0.38	−0.36	−0.08	0.22	0.07	−0.51
$\log \mathrm{T}_r$	7.870	9.583	8.428	8.223	8.672	7.789	9.037	7.938
$\log\rho_\circ$	5.024	3.347	3.856	4.109	3.556	4.475	2.017	4.381
$\mathrm{V_{HB}}$	14.06	14.52	15.68	16.25	14.95	13.8	15.3	15.10
$B/(B+R)$	$0.1^{\ddagger\ddagger}$	$0.9^{\ddagger\ddagger}$	$0.37^{\ddagger\ddagger}$	$0.47^{\ddagger\ddagger}$	$0.97^{\ddagger\ddagger}$	$1.0^{\ddagger\ddagger}$	0.95	$0.92^{\ddagger\ddagger}$
$(\mathrm{m}-\mathrm{M})_V$	$13.4^{\S}$	13.82^{**}	14.97^{**}	$14.3^{\dagger\dagger}$	$14.5^{\ddagger}$	13.03^{**}	14.9^{*}	$14.6^{\dagger}$
$\mathrm{E}(B-V)$	$0.04^{\S}$	0.11	0.00	$0.02^{\dagger\dagger}$	$0.00^{\ddagger}$	0.04^{**}	0.015^{*}	$0.02^{\dagger}$
[Fe/H]	$-0.65^{\S}$	-1.59^{**}	-1.66^{**}	$-1.13^{\dagger\dagger}$	$-1.4^{\ddagger}$	−1.39	-1.4^{*}	$-2.03^{\dagger}$
Age	20.9^{**}	21.4^{**}	18.7^{**}	18.3^{**}	19.1^{**}	20.9^{**}	20.0^{**}	20.9^{**}

Table 2.2: Properties of some galactic globular clusters. The left column is the same as Table 2.1, except: Age in Gyr as determined by Buonanno, *et al.* (1989). All references: Webbink (1985), except *Bolte (1989b), †Stetson and Harris (1988), ‡Richer and Fahlman (1986), ††Richer and Fahlman (1987), ‡‡Zinn (1980), §Hesser, *et al.* (1987), **Buonanno, *et al.* (1989).

Chapter 3

Data

Images for three fields near M10 were obtained at the Canada-France-Hawaii 3.6 m Telescope. These fields are referred to as the *Inner* Field, *Field 2* and the *RCA2* Field. Table 3.1 and Figure 3.1 locate these data with respect to M10. Note that the RCA2 Field is split into 3 portions, two of which are labeled RCA2 Inner Field and RCA2 Outer Field. The very innermost section of the RCA2 data was not used due extreme crowding and saturation. The observing logs are given in Tables 3.2, 3.3 and 3.4. The CFHT Observers Manual contains a description of the instrumentation used.

Field	Image Size	Location with respect to M10 center	Distance from M10 in r_c
Inner	$1'.15 \times 1'.84$	$1'.8$ W	2.34
Field 2	$1'.15 \times 1'.84$	$3'.5$ E	4.55
RCA2	$4'.27 \times 2'.43$	$3'.5$ E	4.55

Table 3.1: Location of images. The RCA2 Field is split into three equal sections. The innermost section is unused due to extreme crowding and saturation. The outer sections are referred to as the RCA2 Inner Field and RCA2 Outer Field. Core radius, $r_c = 0'.77$ from Peterson and King(1975).

Observers:			Fahlman, Richer				
Focus:			Cassegrain ($f/8$)				
Instrument:			RCA1				
Object	Tape	File	Filter	Exp.(sec)	Date	U.T.	Image Name
Std A	5	8	B	20	13/July/85	06:16:53	bstd1
Std A	5	9	B	20	13/July/85	06:19:09	bstd2
Std A	5	10	V	20	13/July/85	06:21:52	vstd1
Std A	5	11	V	20	13/July/85	06:24:08	vstd1
InnerField	5	12	B	30	13/July/85	06:43:52	b short
InnerField	5	13	B	120	13/July/85	06:50:07	
InnerField	5	14	B	120	13/July/85	06:52:56	
InnerField	5	15	B	120	13/July/85	06:57:35	
InnerField	5	16	B	120	13/July/85	07:01:44	
InnerField	5	17	B	120	13/July/85	07:04:32	b
InnerField	5	18	B	120	13/July/85	07:08:05	
InnerField	5	19	B	120	13/July/85	07:10:55	
InnerField	5	20	B	120	13/July/85	07:14:03	
InnerField	5	21	B	120	13/July/85	07:17:04	
InnerField	5	22	B	120	13/July/85	07:20:13	
InnerField	5	23	V	30	13/July/85	07:23:46	v short
InnerField	8	12	V	120	16/July/85	09:25:48	
InnerField	8	13	V	120	16/July/85	09:29:50	
InnerField	8	14	V	120	16/July/85	09:33:02	
InnerField	8	15	V	120	16/July/85	09:36:28	
InnerField	8	16	V	120	16/July/85	09:39:37	v
InnerField	8	17	V	120	16/July/85	09:42:45	
InnerField	8	18	V	120	16/July/85	09:45:28	
InnerField	8	19	V	120	16/July/85	09:48:10	
InnerField	8	20	V	120	16/July/85	09:50:49	
InnerField	8	21	V	120	16/July/85	09:53:35	

Table 3.2: Inner Field data.

Observers:			Fahlman, Richer				
Focus:			Cassegrain ($f/8$)				
Instrument:				RCA1			
Object	Tape	File	Filter	Exp.(sec)	Date	U.T.	Image Name
Std A	6	8	B	20	14/July/85	6:23:13	bstd1
Std A	6	9	B	20	14/July/85	6:25:34	bstd2
Std A	6	10	V	20	14/July/85	6:30:27	vstd1
Std A	6	11	V	20	14/July/85	6:32:01	vstd2
Field 2	6	12	B	30	14/July/85	6:44:04	
Field 2	6	14	B	30	14/July/85	6:58:05	b short
Field 2	6	15	B	30	14/July/85	7:02:17	
Field 2	6	19	V	1200	14/July/85	7:25:57	v
Field 2	7	21	U	2400	15/July/85	6:47:00	u
Std A	7	12	V	20	15/July/85	5:43:21	sa108v20a
Std A	7	13	V	20	15/July/85	5:46:32	sa108v20b
Std A	7	14	V	20	15/July/85	5:49:33	sa108v20c
Std A	7	15	V	20	15/July/85	5:53:26	sa108v20d
Std A	7	16	B	20	15/July/85	5:55:45	sa108b20a
Std A	7	17	B	20	15/July/85	5:58:01	sa108b20b
Std A	7	18	U	60	15/July/85	6:03:28	sa108u60
Std A	7	19	U	300	15/July/85	6:07:49	sa108u300
Std B	7	34	U	300	15/July/85	14:16:28	sa114u300
Std B	7	35	B	30	15/July/85	14:22:48	sa114b300a
Std B	7	36	B	30	15/July/85	14:24:17	sa114b300b
Std B	7	37	V	10	15/July/85	14:25:53	sa114v10a
Std C	7	38	V	20	15/July/85	14:29:39	sa115v20a
Std C	7	39	B	30	15/July/85	14:31:38	sa115b30a
Std C	7	40	U	300	15/July/85	14:36:11	sa115u300a
Std D	7	41	U	120	15/July/85	14:44:15	gdu1200a
Std D	7	43	B	30	15/July/85	14:54:15	gdb30a
Std D	7	44	V	30	15/July/85	14:55:88	gdv30a
Field 2	8	9	B	1200	16/July/85	8:23:26	b

Table 3.3: Field 2 data.

Observers:				Nemec, Richer			
Focus:				Prime ($f/3.77$)			
Instrument:				RCA2			
Field	Tape	File	Filter	Exp.(sec)	Date	U.T.	Name
RCA2 Field	17	2	V	900	30/Apr/87	11:39:04	
RCA2 Field	17	3	V	900	30/Apr/87	11:55:32	v
RCA2 Field	17	4	V	60	30/Apr/87	12:12:43	v short
RCA2 Field	17	5	B	60	30/Apr/87	12:15:38	b short
RCA2 Field	17	6	U	3600	30/Apr/87	12:29:49	u
RCA2 Field	17	7	B	900	30/Apr/87	13:51:15	
RCA2 Field	17	8	B	900	30/Apr/87	14:07:43	b

Table 3.4: RCA2 data.

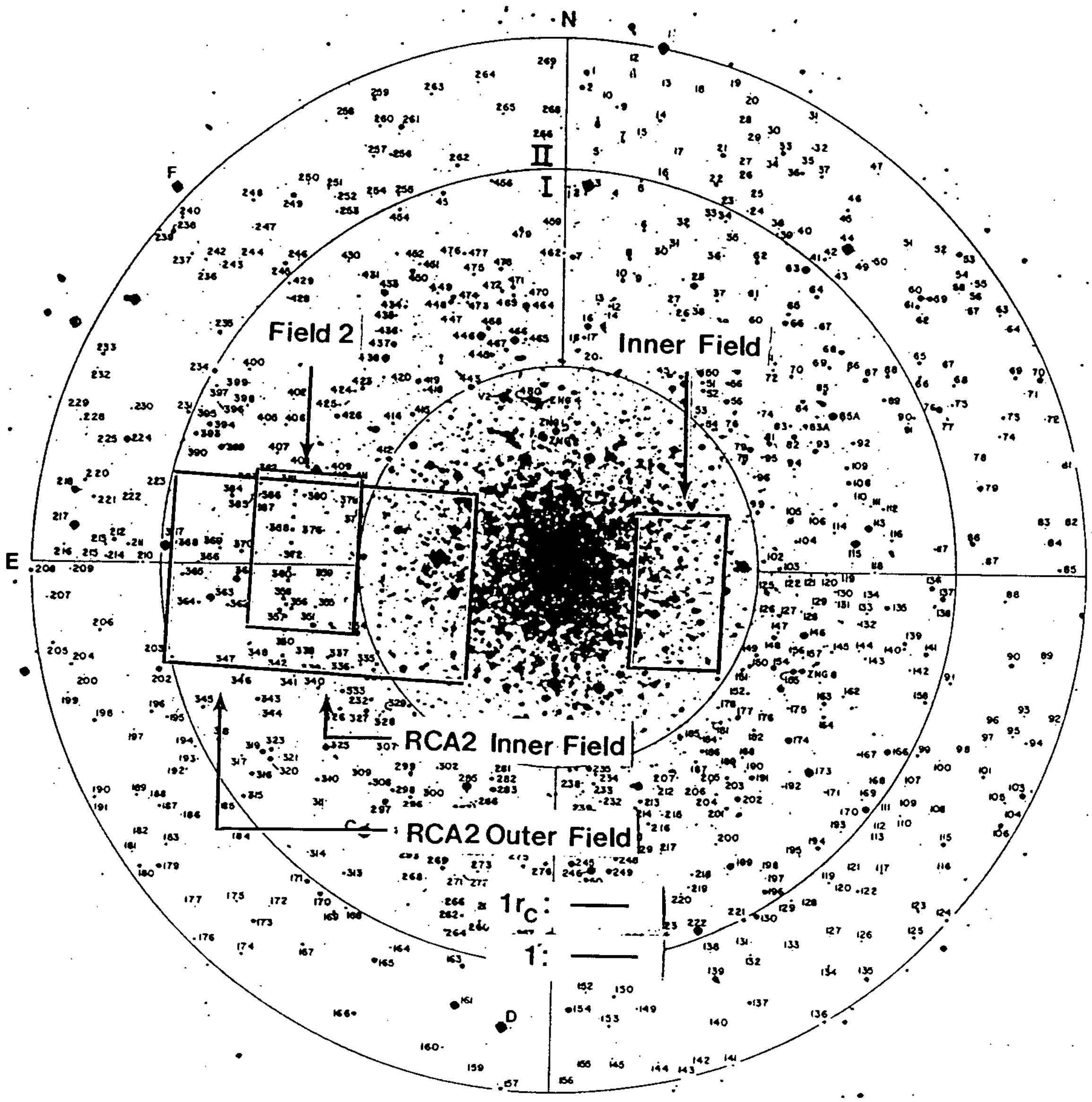

Figure 3.1: Location of images. Figure is reproduced with permission from Harris, Racine and deRoux (1976). Bars corresponding in length to one core radius (0.′77) and 1′ appear in the lower part of the figure.

Chapter 4

Data Reduction

4.1 DAOPHOT

DAOPHOT is a computer program developed to perform photometry in crowded images. The primary reference for DAOPHOT is Stetson (1987).

A typical DAOPHOT reduction sequence consists of a series of the following steps:

Finding The image is convolved with a Gaussian approximating the stellar profile. The convolved image is searched for intensity enhancements greater than a user supplied threshold. Intensity enhanchements exceeding this level are then examined to determine ***roundness*** and ***sharpness*** criteria. Any bright area which falls in the specified roundness and sharpness range is taken to be a star. The star is then centroided and its coordinates are entered into a data file. If the threshold level is set too high, the possibility exists of leaving many real stars uncatalogued. If the threshold is too low, detector readout noise and photon counting statistics may be mistaken for dim stars.

Aperture Photometry Aperture photometry is performed on each candidate star found above. The resulting magnitudes are recorded in a data file.

Grouping Since the profile-fitting routine which follows can only accomodate a small number of stars at once, the stars are collected into groups. The version of DAOPHOT used here allowed a maximum group size of 60. In grouping, a group radius is selected which must be large enough so that stars which contribute light to their neighbours are grouped together, and small enough that the group size does not exceed 60 members.

Profile Fitting Fitting proceeds one group at a time, i.e. the solutions for any two groups are independent. A point spread function (PSF) is fitted to all stars in the group simultaneously. The quality of the fit is then evaluated and if this value is not good enough, the star parameters are modified and the fit redone. This iteration repeats until a user supplied maximum of iterations is reached, or until the solution converges to within certain criteria. Typically the maximum iterations allowed is about 25, though in many cases 10 is sufficient. The solution for each group consists of two position coordinates and a magnitude for each star, and an overall sky value for the group. For each star the magnitude, sky value and a goodness of fit parameter χ^2 are stored.

The reader is directed to Stetson (1987) for a thorough discussion of point spread functions. However it is important to emphasize one point. The PSF for a frame *must come from that frame.* The PSF is affected by guiding errors and rapid variations in seeing. Therefore it is not possible to use a PSF from one image to reduce another. This means that in very crowded images the PSF must be developed from stars in that crowded image.

Image Subtraction The stars found and measured can now be subtracted from the original image. This provides a diagnostic for the quality of the profile fitting and can reveal additional dim stars hidden in the wings of bright stars.

The FIND routine can then be performed on the subtracted image to identify the previously hidden stars. The sequence of events is continued until all star-like images on the frame have been identified and removed.

4.1.1 DAOPHOT Parameters

Some of the more important DAOPHOT parameters are:

FWHM — The Full Width at Half Maximum actually only directly affects the FIND routine, which in turn can affect the rest of the reduction. The FWHM provides the initial guess for the kernel used in the FIND convolution. The FWHM was set to be about 0.8 times the true full width at half maximum, except in the case of the very crowded Inner Field. In the Inner Field the FWHM was set to 0.6 times the true full width at half maximum.

Fitting Radius Determines how much of the core of the star is considered in the fit. The fitting radius must include enough of the star to enclose sufficient pixels for a reasonable fit. In this work, fitting radius = 0.8 FWHM .

PSF Radius The size of the PSF. If the PSF radius is too small, subtracted stars may leave rings as the cores are removed but not the wings. In this work, PSF radius = 3 FWHM.

Photometry Aperture In this study the aperture radius = 0.6 FWHM. The output from the photometry routine only provides an initial guess to the profile-fitting routine.

4.2 The Data Fields

4.2.1 Inner Field

The extreme crowding at $1\overset{'}{.}8$ from the center of M10, combined with relatively poor seeing ($1\overset{''}{.}5$), made the Inner Field very difficult to reduce. When stars are too close, the DAOPHOT profile fitting routine may merge them into one, even if they are identified as separate stars by the FIND routine. The only warning that this has happened is a very high goodness-of-fit parameter, $\chi^2 \geq 10$, for the returned star.

The following reduction scheme was adopted for the Inner Field:

1. A standard reduction is performed as outlined in §4.1.

2. Stars with a DAOPHOT χ^2 parameter greater then 2.0 are rejected.

3. The remaining stars are subtracted from the image.

4. Steps 1 to 3 are repeated on the subracted image, until only a handful of stars are returned; 5 times for *B* and 10 times for *V* in the Inner Field.

5. Two reductions are performed on the final subtracted image, first with $\chi^2 \leq 5.0$ then with $\chi^2 \leq 6.5$. This essentially "scrapes the image clean".

6. Stars are "sieved", retaining only one star from any collection of stars which are within 1.5 pixels of each other. In the sieve routine the star with the lowest value of χ^2 is kept, except when the difference in χ^2 is less than 1.0. In such a case the star with the lowest photometric error is retained.

7. Stars with $\chi^2 \geq 3.0$ are dropped, and this list is used to provide the initial positions and magnitudes for profile fitting on the original frame.

8. Steps 6 and 7 are repeated once more. In this way all the little bits and pieces of light found in the "scraping" are gathered up into stars.

Both B and V colors for the Inner Field were reduced.

4.2.2 Field 2

An essentially standard approach, with two passes, was taken to reducing this frame in U, B and V.

As seen in Figure 3.1, Field 2 almost completely overlaps the RCA2 Field. The Field 2 data, along with the RCA2 data, were used to produce the V versus $(B - V)$ color-magnitude diagram, and to calibrate the RCA2 data. The Field 2 U data were used only to calibrate the RCA2 U frame. Luminosity functions were not generated from Field 2; however, the luminosity function of that part of the RCA2 Field in common with Field 2 was studied.

4.2.3 RCA2 Field

The RCA2 data were obtained during a different observing run than the previous data. These data were obtained with the CHF RCA2 CCD at prime focus.

To enhance its quantum efficiency the glass backing was removed from the RCA2 CCD. An appreciable gain in quantum efficiency in the blue is realized, however removal of the glass backing allowed the photosensitive surface to wrinkle. The RCA2 CCD displays a distinct ripple pattern (which manifests itself as a varying point spread function) as its surface varies in distance from the focal plane. Unfortunately, this pattern is quite complex and not well modelled by simple bilinear variations in the PSF, as recent versions of DAOPHOT support.

The RCA2 data were reduced as in §4.1, with no special allowances for a varying PSF. The RCA2 data were obtained under non-photometric conditions; however, this field overlapped with the Field 2 data, so calibration was possible. The RCA2 data spans from about 1!4 to 5!6 from the core. These data are therefore much more crowded at one end than the other. The less crowded end and center area were used to produce the color magnitude diagram, and luminosity functions Both the least crowded end and the center portion of the field were used to produce luminosity functions. A luminosity function was not generated for the most crowded end. To illustrate the effect of crowding on the quality of photometry, V versus $(B-V)$ color-magnitude diagrams were produced for various distances from the cluster center; the results are shown in Figure 4.1.

Short exposure data were available for the RCA2 Field in both B and V. These data were reduced as per §4.1 and were used for the brighter stars in the V versus $(B-V)$ and the $(U-B)$ versus $(B-V)$ color-color diagram and the bright portions of the color magnitude diagram.

4.3 Calibration

Data for all fields were obtained in both B and V of the Johnson UBV system. Data for Field 2 and RCA2 were also secured in U. CCD images in these bands were also obtained of standard stars. Landolt standards SA 108−719,727,728 (Standard Field A), SA 114−548 (Standard Field B), SA 115−486 (Standard Field C) and GD426 (Standard Field D) were used. See Landolt (1973,1983) for colors and magnitudes of these stars.

The usual procedure for transforming the results of the profile fitting to the UBV system involves obtaining aperture photometry of the standard stars and establishing a set of transformation equations. Assuming photometric observing conditions, these transformations can then be applied to all stars on the program frames whose magnitudes can be determined by aperture photometry. In practice, it is often impossible to perform aperture photometry on the program frames due to crowding. To circumvent this problem, short exposure images are obtained of the program fields. Aperture photometry can then be performed on these less crowded short exposure frames. B and V magnitudes are determined for these stars, referred to as secondary standards. Since these stars have magnitudes determined for them on the program frames through profile fitting (known as NSTAR magnitudes), final transformations from the NSTAR magnitudes to Johnson magnitudes can be obtained. The transformations have the form

$$
\begin{aligned}
(B - V) &= \alpha_c + \beta_c(b_\star - v_\star) \\
(V - v_\star) &= \alpha_v + \beta_v(B - V) \\
(U - u_\star) &= \alpha_u + \beta_u(U - B)
\end{aligned}
\tag{4.1}
$$

where U,B and V represent Johnson magnitudes, and $u_\star$, $b_\star$ and $v_\star$ represent magnitudes determined from profile fitting. Since no b and v data were obtained at the same time as the u data in Field 2, there is no $(U - B)$ transformation in terms of $(u - b)$.

In some of the plots described in the following sections some stars were not considered. The method of rejecting outliers was to drop points until the average deviation from the fit satisfied $\overline{\sigma} \leq 0\overset{\text{m}}{.}05$.

4.3.1 Inner Field

The Inner Field was calibrated only in B and V. The calibration was based on Standard Field A, as described in §4.3. With only three stars the β coefficients of Equations 4.1 are poorly determined. The β coefficients have instead been fixed at the values from CFHT Observers Manual: $\beta_c = +1.26$, $\beta_v = -0.060$.

From aperture photometry of the standard stars, the tranformations to the Johnson system for the standard star aperture photometry were found to be:

$$
\begin{aligned}
(B - V) &= +0.471 + 1.26(b - v) \\
(V - v) &= -7.541 - 0.060(B - V)
\end{aligned}
$$

These equations are plotted against the data in Figure 4.2. Airmass and extinction corrections were first made to the aperture photometry results. Extinction coefficents of 0.15 in b and 0.11 in v, taken from the CFHT Observers Manual, have been used throughout this work. All aperture exposure times in this section have been normalized to one second. Aperture photometry was performed on approximately thirty stars on the short exposure frames. The light from the stars was measured out to 6 pixels. Aperture corrections to extrapolate the magnitudes measured at 6 pixels to 20 pixels (assumed large enough to contain all the light from the star), were found to be $0\overset{\text{m}}{.}097$ magnitudes in b and $0\overset{\text{m}}{.}11$ magnitudes in v. i.e. $b = b_{\text{ap}} - 0.097$ and $v = v_{\text{ap}} - 0.11$.

The transformations from profile fitting to Johnson system photometry are shown in Figure 4.3 and are:

$$\begin{aligned}(B-V) &= -4.284 + 1.26(b_\star - v_\star) \\ (V - v_\star) &= -3.410 - 0.06(B-V)\end{aligned} \tag{4.2}$$

4.3.2 Field 2

4.3.2.1 B and V Calibration

From Standard Field A, described in §4.3, the following transformations were derived to transform aperture photometry to Johnson system photometry. These transformations are plotted in Figure 4.4.

$$\begin{aligned}(B-V) &= +0.419 + 1.26(b - v) \\ (V - v) &= -7.539 - 0.060(B-V)\end{aligned}$$

As with the Inner Field calibration the color dependency coefficients were again taken from CFHT Observers Manual. Aperture correction terms of $0\overset{m}{.}26$ in b and $0\overset{m}{.}14$ in v were used.

As no short exposure data were available for V, few uncrowded stars were available on this frame. Candidate stars for aperture photometry were selected and nearby stars were subtracted away. This technique worked satisfactorily and the following transformations were obtained for profile fitting photometry, which are illustrated in Figure 4.5.

$$\begin{aligned}(B-V) &= 0.007 + 1.26(b_\star - v_\star) \\ (V - v_\star) &= -0.478 - 0.06(B-V)\end{aligned} \tag{4.3}$$

It is noteworthy that the derived tranformations in $(V-v)$ versus $(B-V)$ for both the Inner Field and Field 2 are not good fits to Landolt's standard star data. However, both fields produce virtually identical fits to the data. Figures 4.2, 4.4 and 4.6 suggest that the B and V photometry of SA 108−719 may be in error.

4.3.2.2 U Calibration

For the U calibration sufficient standards were observed to allow independent determination of the color dependency coefficients. A full three color UBV transformation is derived. However only the U transformation will be used further. The following transformations were derived to transform aperture photometry to Johnson. The transformations are plotted in Figure 4.6:

$$\begin{aligned}(B-V) &= +0.429 + 1.255(b-v) \\ (V-v) &= -7.591 - 0.037(B-V) \\ (U-u) &= -9.819 - 0.026(U-B)\end{aligned}$$

U band aperture and profile fitting photometry was obtained for many of the secondary standards for which B and V photometry had been obtained. This three color photometry lead to the following transformations which are plotted in Figure 4.7.

$$\begin{aligned}(B-V) &= 0.015 + 1.26(b_\star - v_\star) \\ (V-v_\star) &= -0.531 - 0.037(B-V) \\ (U-u_\star) &= -2.601 + 0.026(U-B)\end{aligned} \tag{4.4}$$

4.3.2.3 *UBV* Transformations

The B and V transformations derived in §4.3.2.2 are not applicable to the program B and V images upon which aperture photometry was performed, since these images were obtained on separate nights. Only the U transformation equation from §4.3.2.2 is of further use. Combining the the $(B-V)$ and $(V-v_\star)$ transformation equations from Equations 4.3 with the $(U-u_\star)$ transformation equation of Equations 4.4 gives final Field 2 transformations of :

$$\begin{aligned}(B-V) &= 0.007 + 1.26(b_\star - v_\star) \\ (V-v_\star) &= -0.478 - 0.06(B-V) \\ (U-u_\star) &= -2.601 + 0.026(U-B)\end{aligned} \tag{4.5}$$

4.3.3 RCA2

The RCA2 data were obtained under non-photometric conditions. However the overlap between the RCA2 Field with Field 2 provides several tens of stars in common. By matching these common stars, offsets in magnitude were found for RCA2 UBV data and B and V short exposure data these offsets are illustrated in Figure 4.8. With these offsets and the Field 2 UBV transformations from Equation 4.5, transformations for the RCA2 deep data were derived.

$$\begin{aligned}(B-V) &= 0.637+1.26(b_\star-v_\star)\\(V-v_\star) &= -0.588-0.06(B-V)\\(U-u_\star) &= -1.636+0.026(U-B)\end{aligned}$$

Similarly BV transformations were derived for the short exposure data.

$$\begin{aligned}(B-V) &= 0.272+1.26(b_\star-v_\star)\\(V-v_\star) &= -3.328-0.06(B-V)\end{aligned}$$

4.4 Artificial Star Tests

Modern detector technology has made it possible to detect stars below 25^{th} magnitude, in reasonable integration times under good seeing conditions. In an ideal situation every star of every magnitude would be detectable, down to the detection limit. In that case, the construction of a luminosity function would simply involve counting the number of stars in a given magnitude bin. In a more realistic situation not all stars will be detectable. This requires steps be taken to estimate the number of stars not counted and that an estimate of the uncertainty in the number of stars observed, and inferred, be obtained.

A reduction of any given image of a crowded star field will very probably not find and identify every star in that particular area of sky. It is even less likely that all the stars identified will have their magnitudes correctly determined. Whether or not a star is identified is a combination of many factors, in both hardware and software. At the telescope, such factors as detector quantum efficiency, exposure time, seeing and detector readout noise will determine how faint a star can be detected. In processing of the images many more subtle factors contrive to determine how faint a star can be detected. Such factors include the quality of flat-fielding, debiasing and defringing, the accuracy of the point spread function and the environment of a star on the frame; i.e., how crowded that area of the image is. As an example, in DAOPHOT the FIND threshold will determine how faint a star can be found. The lower the FIND threshold the more stars are found; however, the number of spurious detections due to noise may increase dramatically. To construct a true luminosity function, one must be able to estimate how many stars are not being recovered at any magnitude. In practice the range of magnitudes is broken into bins.

An estimator of the completeness of star recovery may be obtained from artificial star tests. In this approach "artificial" stars (scaled replications of the PSF) are added to the image and a reduction identical to that performed on the original frame is carried out. From the resulting stellar photometry list the ratio of stars added to stars recovered can be determined for each magnitude bin. What constitutes a recovered star is discussed in §4.4.1.

The artificial star test is an effective method for determining incompleteness; however, it has a number of drawbacks. Adding artificial stars alters the image being reduced. The incompleteness factors found are more applicable to the image with stars added (i.e. slightly more crowded) than for the original. This is unavoidable but may be minimized by adding only a few stars at a time. In practice, about 10% of the total number of stars recovered from the original image may be added safely. Since only a few stars can be added at a time and uncertainties in the recovery probability in any given bin will get smaller as the number of stars added to that bin increases, several reductions on images with artificial stars may have to be performed to reduce the uncertainties in any given bin to a acceptable level. Another serious problem with the artificial star test method is that the stars added are generated from the point spread function used for the image. This means that stars added are identical to the PSF assumed for the image, while real stars on the image may not be, due to the combined effects of noise and an imperfectly known PSF.

4.4.1 Recovered Stars

The observed photometry list, added star list and recovered photometry list are matched. If a star is added near another star and appears on all three lists it is a *triple match.* When the added and recovered magnitudes were similar and distinct from the observed magnitude the triple match is counted as a recovery, otherwise it is not. For the purpose of examining photometric errors (§4.4.2), all matches between stars on the added list and recovered list (*double matches*) are counted as recoveries. In many cases a star added at one magnitude is recovered at another, this phenomena of *bin jumping* is discussed by Drukier, *et al.* (1988) and Stetson and Harris (1988). It is as yet unclear if corrections for bin jumping should be made in cases of shallow luminosity functions, and if so, what technique to use. Bin jumping is not formally addressed in this work, however its effect is commented upon further in §5.7.

In order to determine the recovery probabilities only those stars recovered within a half magnitude of the magnitude at which they were added were counted as valid recoveries. In the following section on errors in incompleteness (§4.4.3), stars recovered in a bin (N_{rec_i}) refers to stars recovered which are added to that bin, even though these stars may have been recovered in other bins, and *jumped* out of the bin under consideration.

4.4.2 Photometric Errors

A series of artificial star tests is an effective diagnostic of photometric accuracy. The difference in magnitude at which stars are added and recovered over a given magnitude range gives a good indication of how accurate the photometry over that magnitude range is. In the case of a crowded image this measure of photometric accuracy is certainly more relevant than photometric errors derived from Poisson statistics applied to the number of photons from the star. Figure 4.9 shows the photometric errors for the recovered stars in the Inner Field. Steps taken in reducing the Inner Field to avoid detecting remnants of subtracted stars as real stars resulted in the loss of many real stars at faint magnitudes. The Inner Field data only just extends to $V = 20$, however the errors down to this level are well under control. The RCA2 Field was split into three parts; the innermost of which was not processed due to severe crowding and saturation. Figures 4.10 and 4.11 show the photometric errors for the recovered stars in the RCA2 Inner Field and Outer Field, respectively. The RCA 2 Inner Field data extends to $V = 23$, and the RCA2 Outer Field data extends below $V = 24$. However in the case of both RCA2 Fields there is rather wide scatter at the faint end.

4.4.3 Errors in Incompleteness

A quantity may be defined which represents the probability of recovering a star in a given magnitude bin:

$$f_i = N_{rec_i}/N_{add_i} \tag{4.6}$$

where N_{rec_i} and N_{add_i} represent the number of recovered stars attributed to that bin (what constitutes a recovery is explained in §4.4.1) and the number of stars added to that frame in that bin, repectivly. The number of stars in that bin will be

$$N_i = N_{obs_i} f_i^{-1} \tag{4.7}$$

where N_{obs_i} represents the number of stars observed in a given bin. Of N_i stars, the number of members of the cluster is

$$N_{cl_i} = N_i - N_{field_i} \tag{4.8}$$

where N_{field_i} represents the number of field stars. Field stars are stars which happen to be seen in the direction of the cluster but actually belong to the galactic disk and are not cluster members.

We are interested in an entire cluster which will contain fluctuations in its distribution of stars. The number of stars counted in a single image, a small portion of the total area of the cluster, is assumed, within statistical uncertainty, to be representative of the cluster as a whole, at that radius. To estimate the uncertainty in the number of stars observed we assume that the number of observed stars follows a Poisson distribution. The recovery of stars is well described as a binomial experiment, that is an experiment where n independent and identical trials are carried out. The outcome of the experiment is one of only two possibilities, whose probability remains the same through all trials. The uncertainty in the recovered stars can be obtained from the binomial distribution. The number of field stars has been addressed by Ratnatunga and Bachall (1985), who provide estimates of the number of field stars in the direction of many galactic globular clusters. The authors advise caution in using their values. Nevertheless, they have been adopted here to provide some estimate of the contribution of field stars. Ratnatunga and Bachall suggest an uncertainty in N_{field_i} of $N_{field_i}/4$. This is a minor contribution to the overall uncertainties discussed below. Note that the number of added stars is known absolutely, hence there is no uncertainty associated with this quantity.

The luminosity function, Φ, is given by:

$$\Phi_i = N_{cl_i} \pm dN_{cl_i} \tag{4.9}$$

dN_{cl_i} is obtained by taking a differential of Equation 4.8, thus:

$$dN_{cl_i} = f_i^{-1} dN_{obs_i} - N_{obs_i} f_i^{-2} df - dN_{field_i}$$

Adding the contributions to the error in quadrature, so as to represent an rms error dN_{cl_i} becomes:

$$dN_{cl_i} = \sqrt{\left(\frac{dN_{obs_i}}{f_i}\right)^2 + \left(\frac{N_{obs_i}}{f_i^2}df\right)^2 + (dN_{field_i})^2}$$

The Poisson error in N_{obs_i} is $\sqrt{N_{obs_i}}$. The standard deviation in a binomial distribution is $\sqrt{np(1-p)}$ where n is the number of trials and p is the probability of success (recovery). In this situation, the number of trials is the number of stars added and the probability of success is the probability of a successful recovery, i.e. f. The quantity dN_{rec_i} is given by:

$$\begin{aligned} dN_{rec_i} &= \sqrt{np(1-p)} \\ &= \sqrt{N_{add_i}f(1-f)} \\ &= N_{rec_i}\sqrt{\frac{1}{N_{rec_i}} - \frac{1}{N_{add_i}}} \end{aligned}$$

Taking differentials of Equation 4.6 and assuming Poisson errors in N_{obs_i}, binomial errors in N_{rec_i}, an error of $N_{field_i}/4$ in N_{field_i} and no uncertainty in N_{add_i} yields:

$$dN_{cl} = \sqrt{\left(\frac{N_{add_i}}{N_{rec_i}}\sqrt{N_{obs_i}}\right)^2 + \left(\frac{N_{add_i}}{N_{rec_i}}N_{obs_i}\right)^2\left(\frac{1}{N_{rec_i}} - \frac{1}{N_{add_i}}\right) + \left(\frac{N_{field_i}}{4}\right)^2}$$

which reduces to

$$dN_{cl_i} = N_i\sqrt{\frac{1}{N_{obs_i}} + \frac{1}{N_{rec_i}} - \frac{1}{N_{add_i}} + \left(\frac{N_{field_i}}{4N_i}\right)^2} \tag{4.10}$$

Therefore, the luminosity function Φ becomes

$$\Phi_i = N_{cl_i} \pm N_i\sqrt{\frac{1}{N_{obs_i}} + \frac{1}{N_{rec_i}} - \frac{1}{N_{add_i}} + \left(\frac{N_{field_i}}{4N_i}\right)^2} \tag{4.11}$$

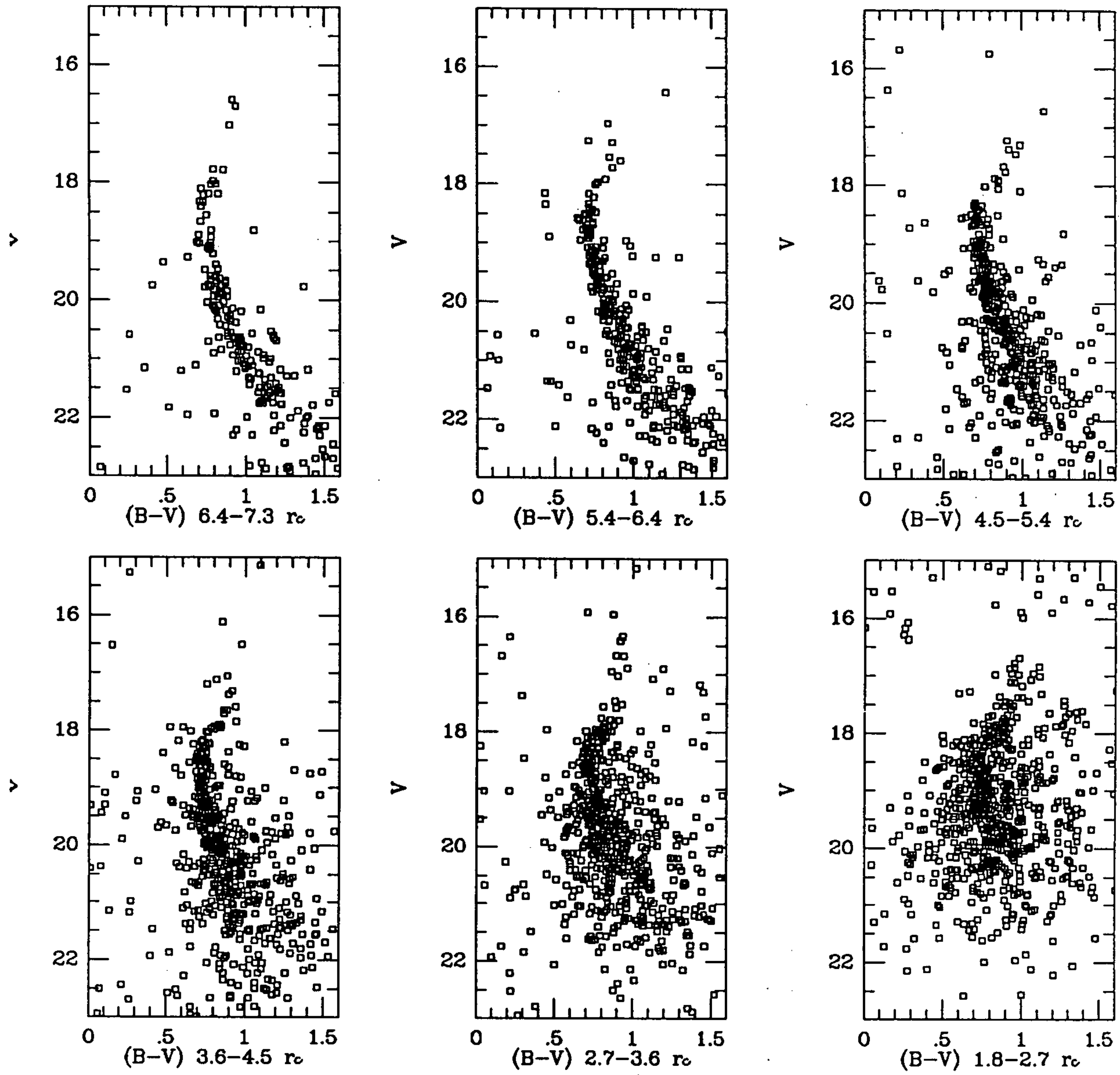

Figure 4.1: Effect of crowding upon RCA2 photometry. Each color-magnitude diagram covers an area of 2!43 by 0!71 radially. From Peterson and King (1975) $r_c = 0'.77$.

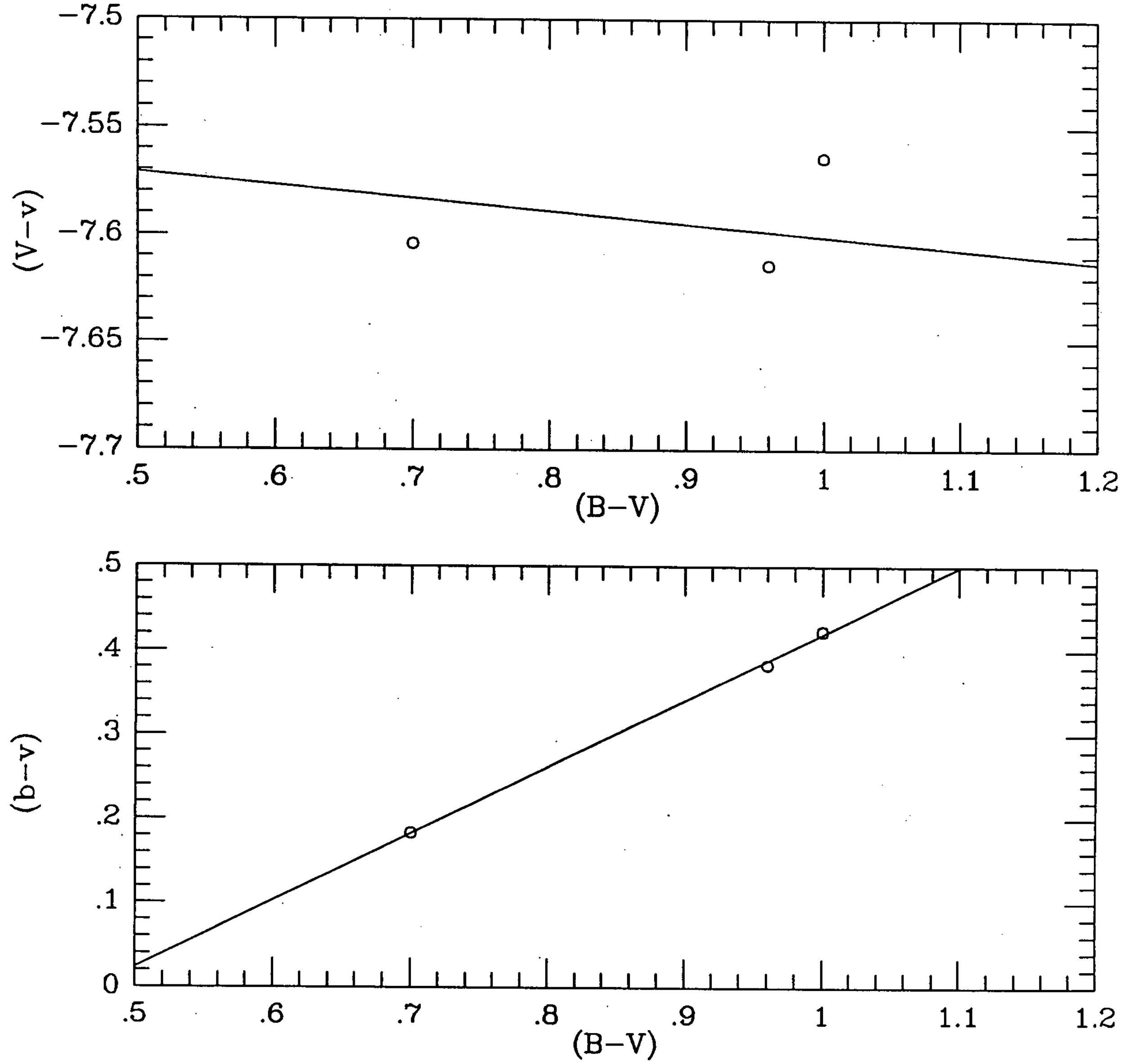

Figure 4.2: Inner Field standard star transformations. The poor fit in $(V - v)$ versus $(B - V)$ is discussed in §4.3.2.1, see §4.3 for standard stars.

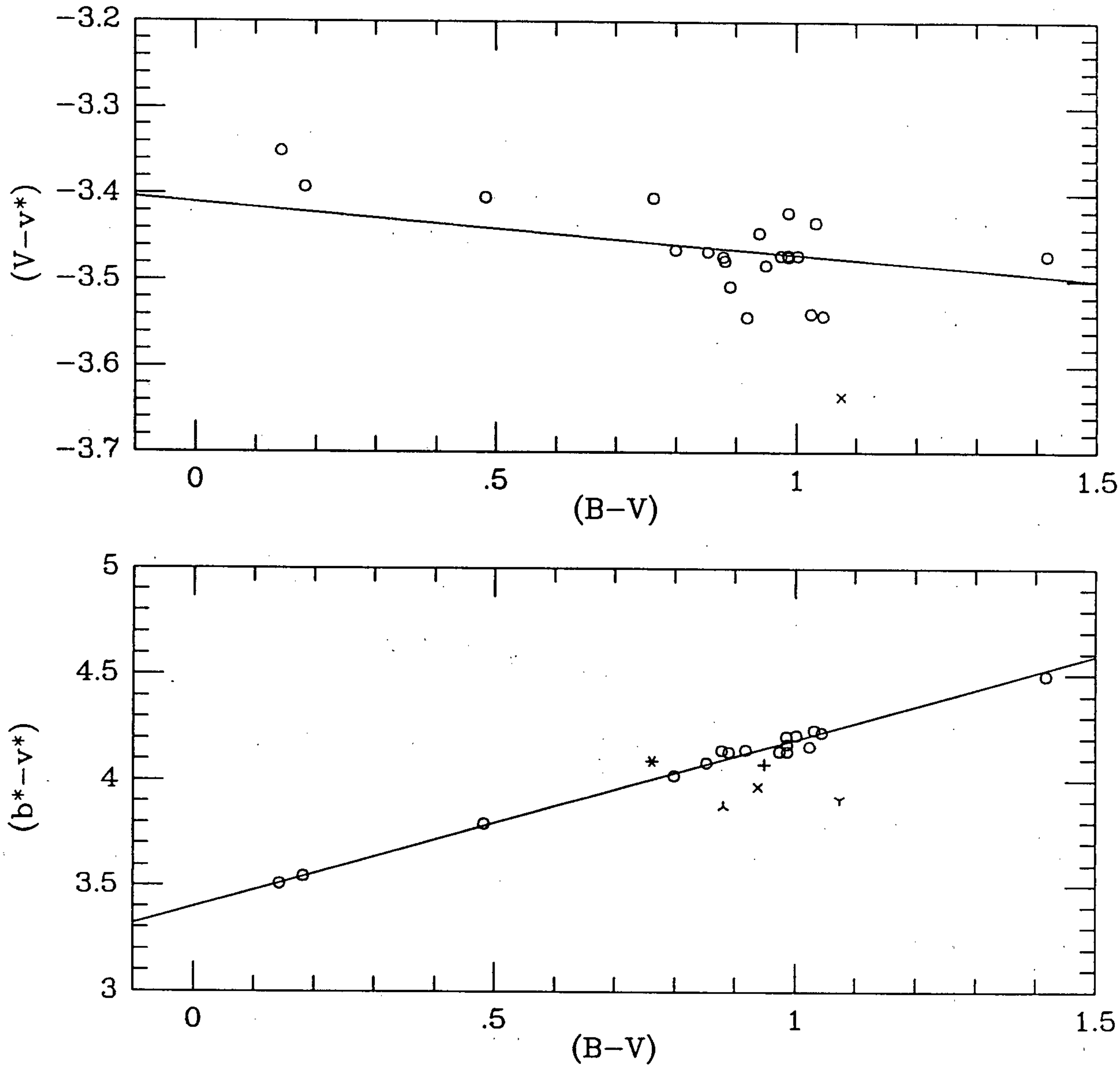

Figure 4.3: Inner Field instrumental magnitude transformations. Open circles denote stars considered in the fit, other symbols represent stars which were dropped.

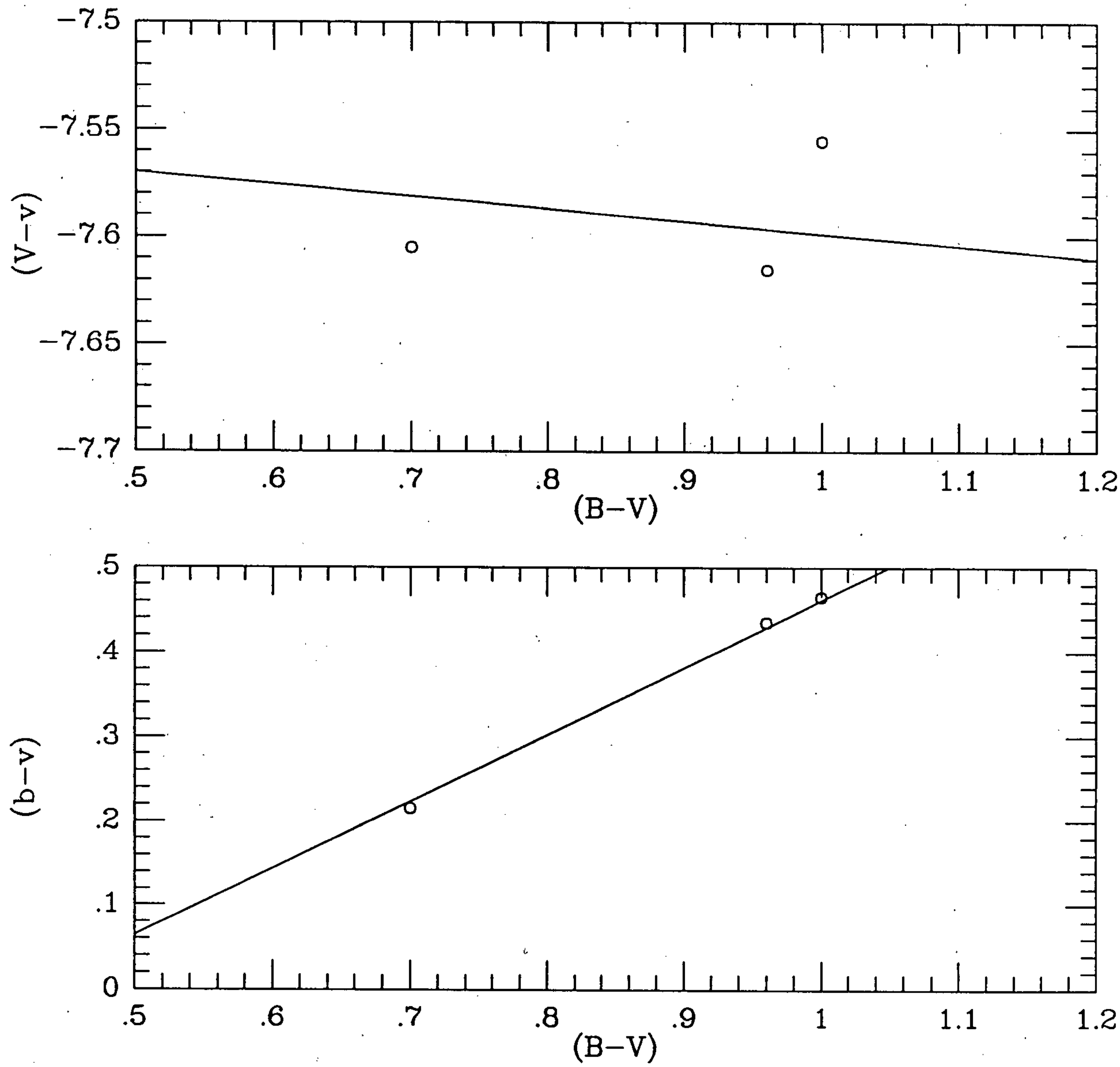

Figure 4.4: Field 2 standard star transformations: B and V. The poor fit in $(V - v)$ versus $(B - V)$ is discussed in §4.3.2.1, see §4.3 for standard stars.

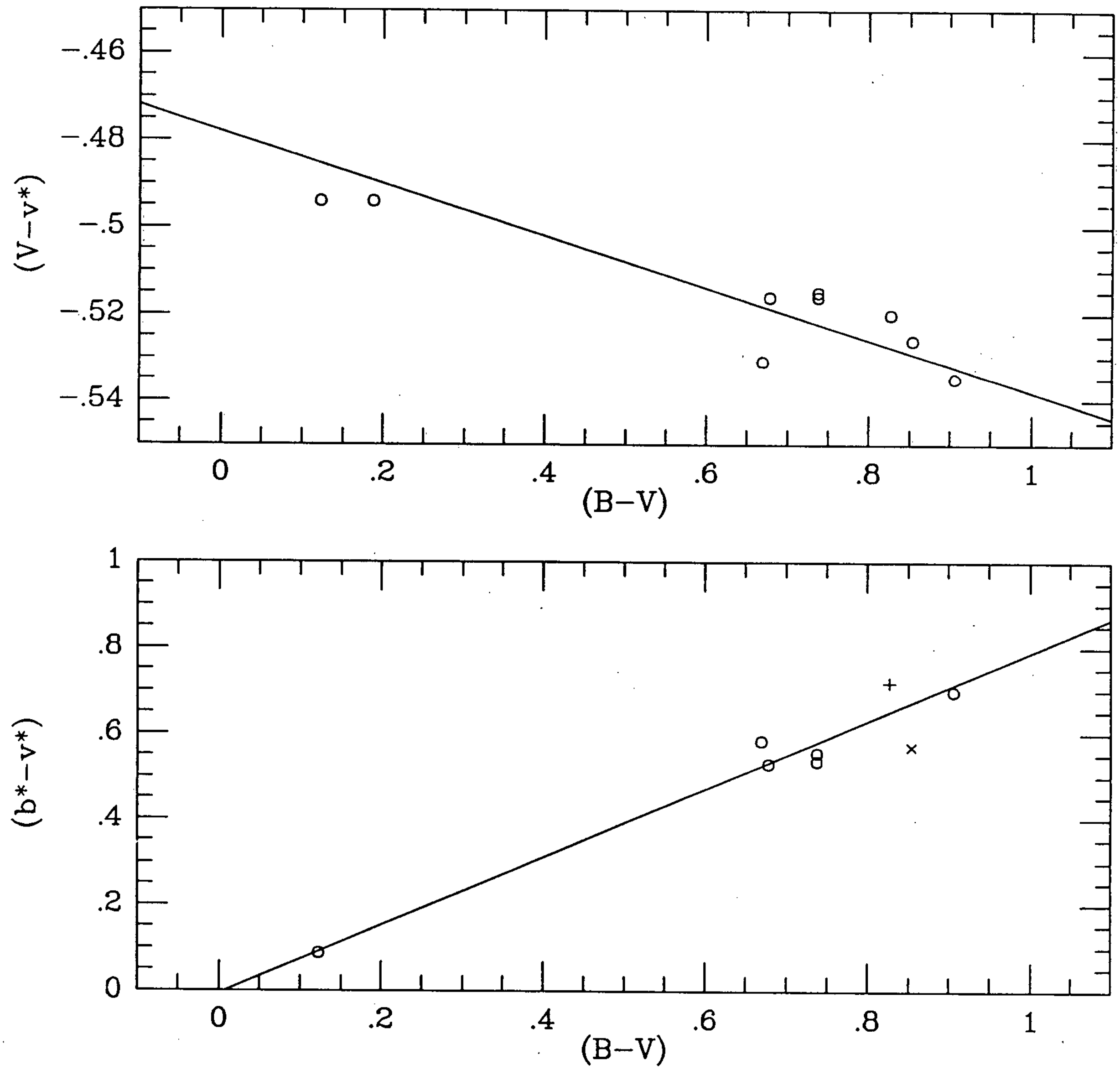

Figure 4.5: Field 2 instrumental magnitude transformations: B and V. Open circles denote stars considered in the fit.

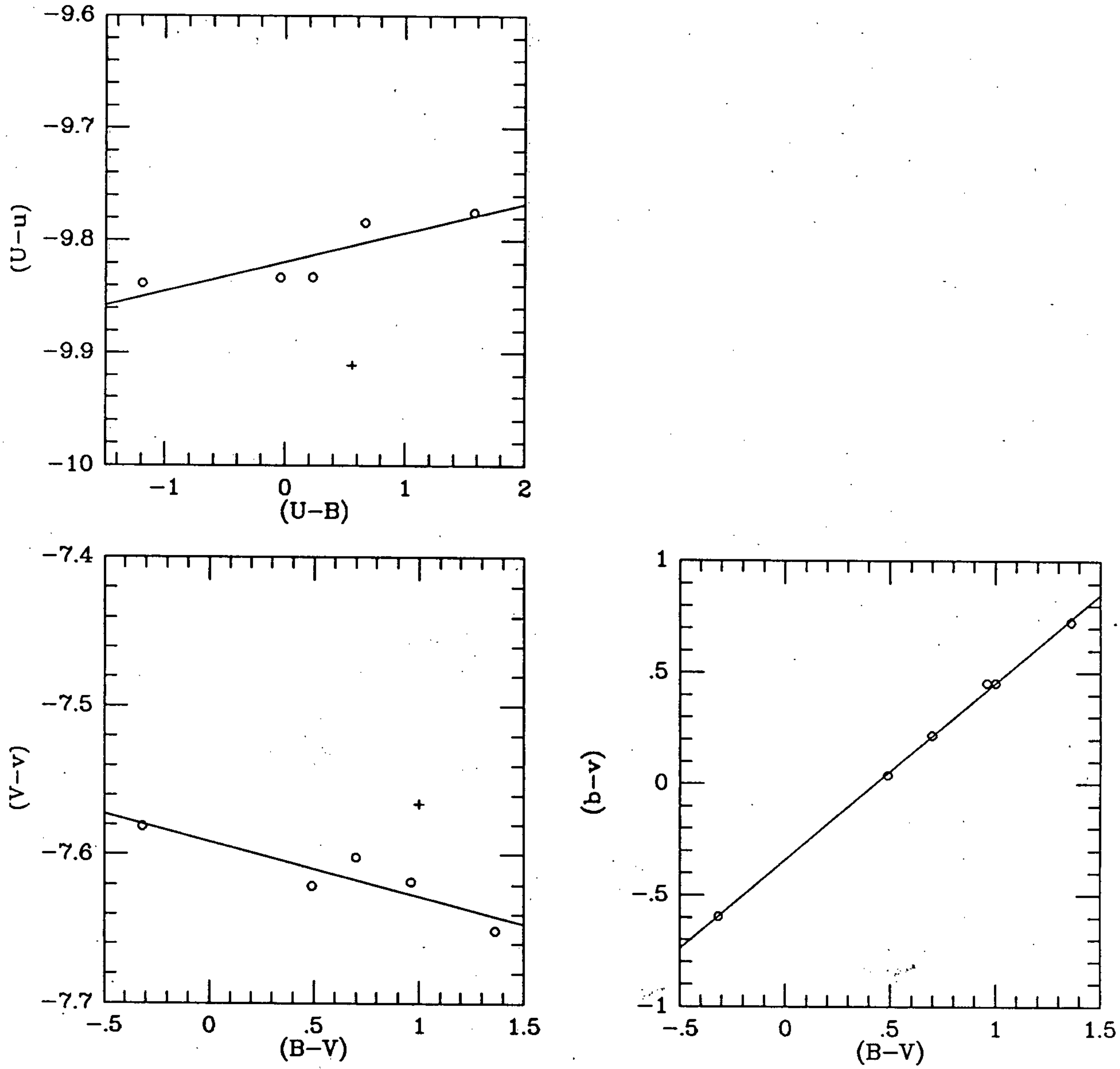

Figure 4.6: Field 2 Standard star transformations: U,B and V. Open circles denote stars considered in the fit, see §4.3 for standard stars.

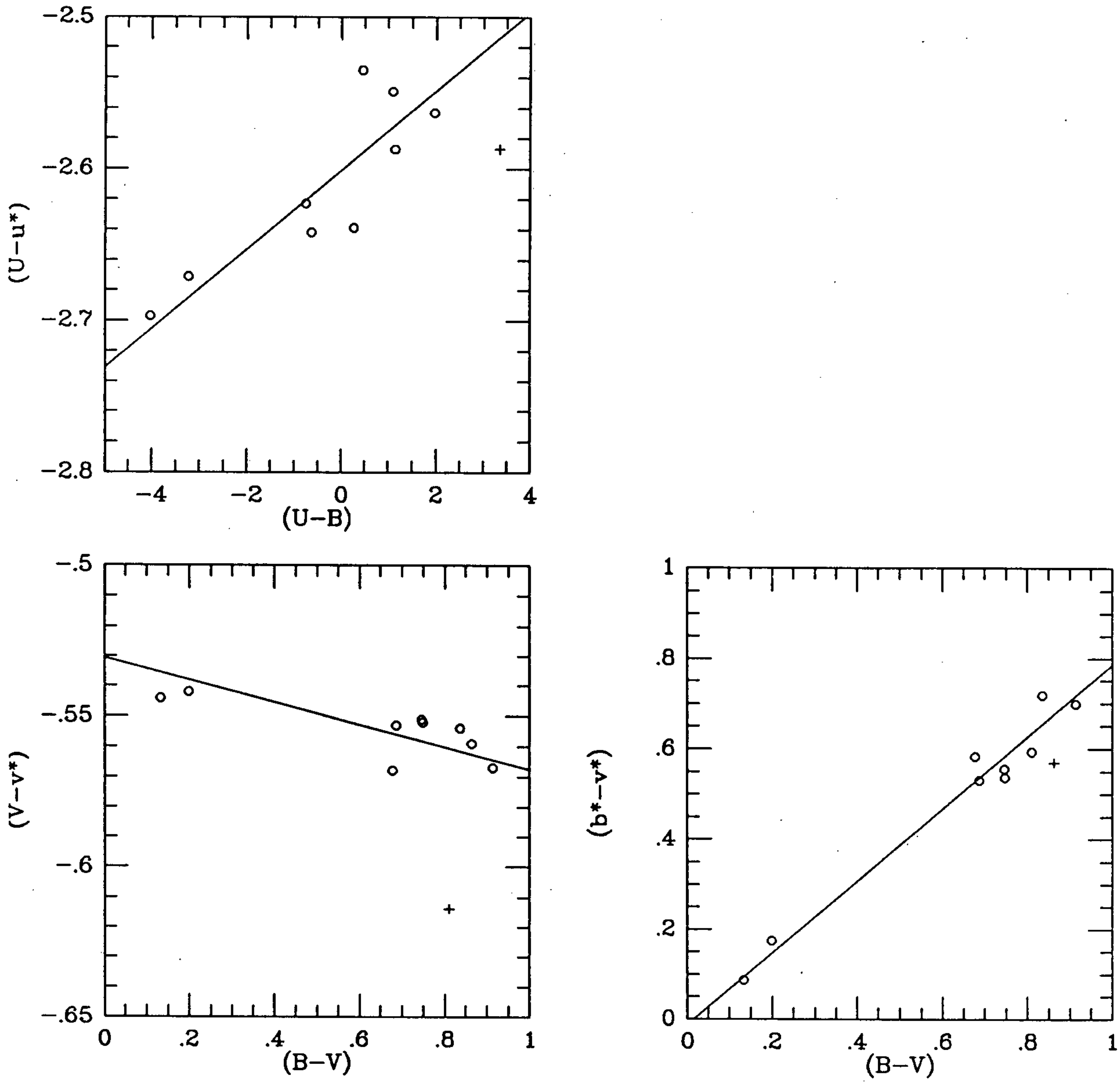

Figure 4.7: Field 2 instrumental magnitude transformations: U,B and V. Open circles denote stars considered in the fit.

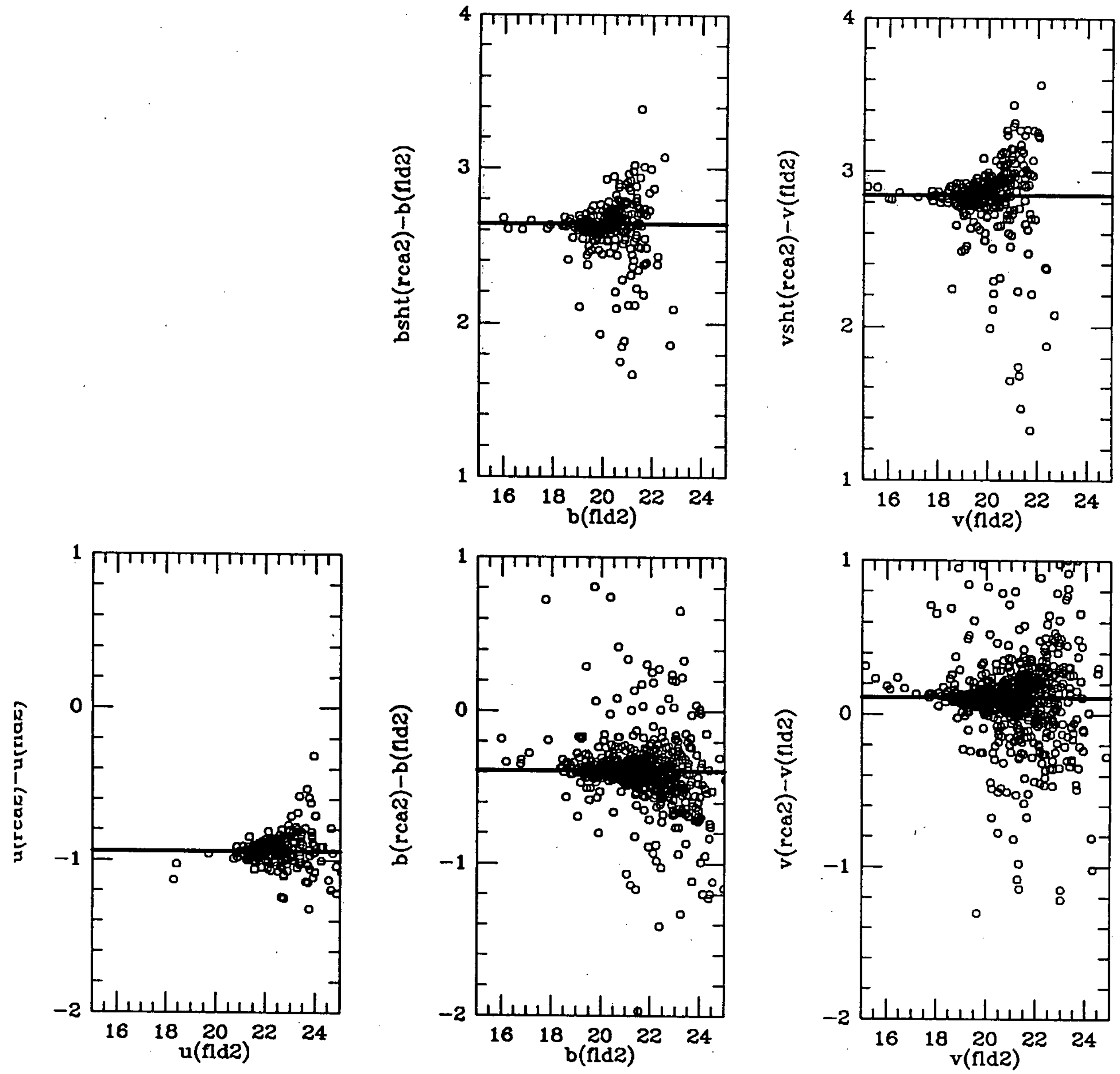

Figure 4.8: RCA2 magnitude corrections. Magnitude corrections are: $u_{\rm RCA2} = u_{\rm Field\ 2} - 0.94$, $b_{\rm RCA2} = b_{\rm Field\ 2} - 0.39$, $v_{\rm RCA2} = v_{\rm Field\ 2} + 0.11$, $b_{\rm RCA2Short} = b_{\rm Field\ 2} + 2.64$, $v_{\rm RCA2Short} = v_{\rm Field\ 2} + 2.85$.

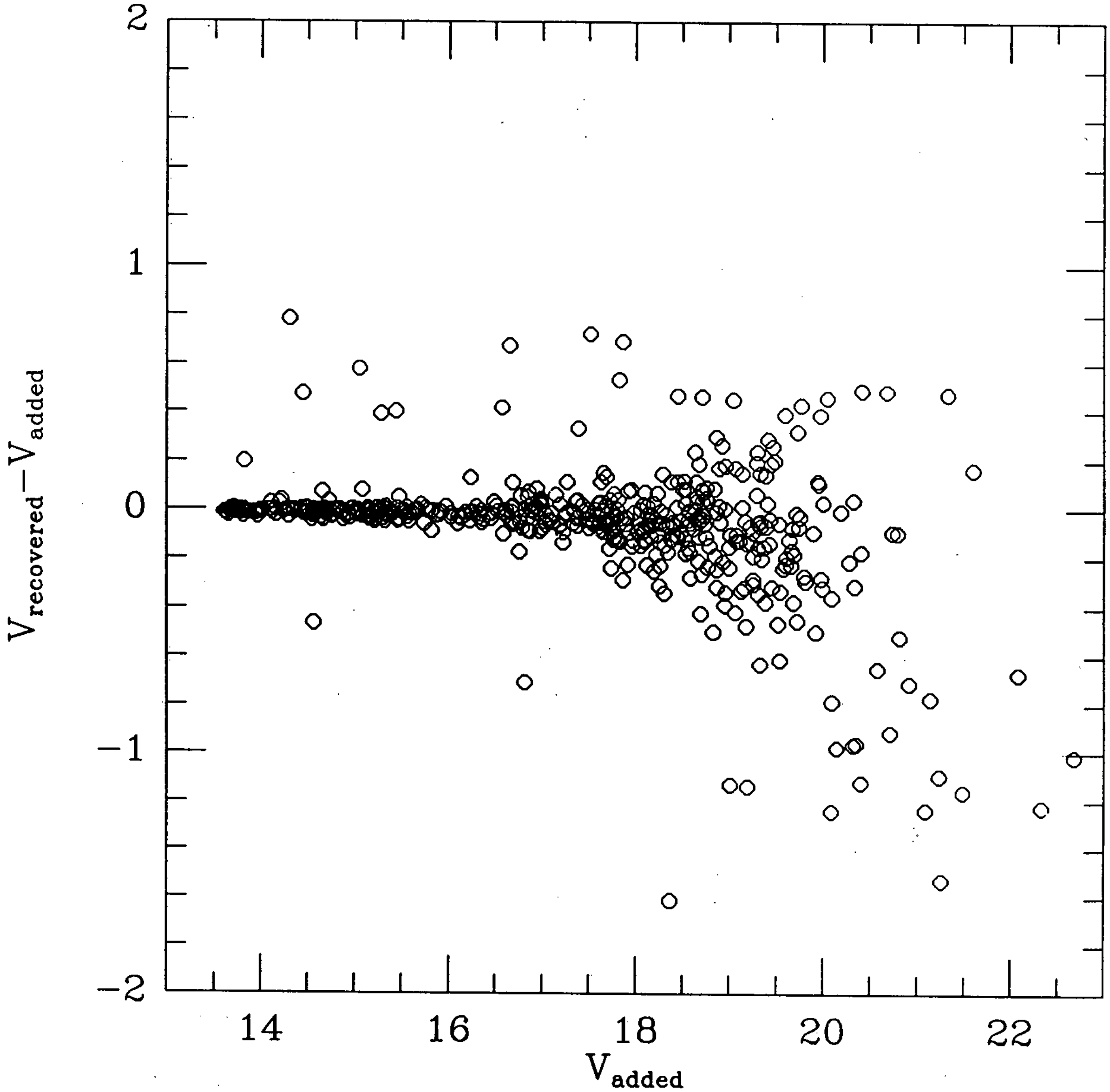

Figure 4.9: Inner Field photometric errors from artificial star tests.

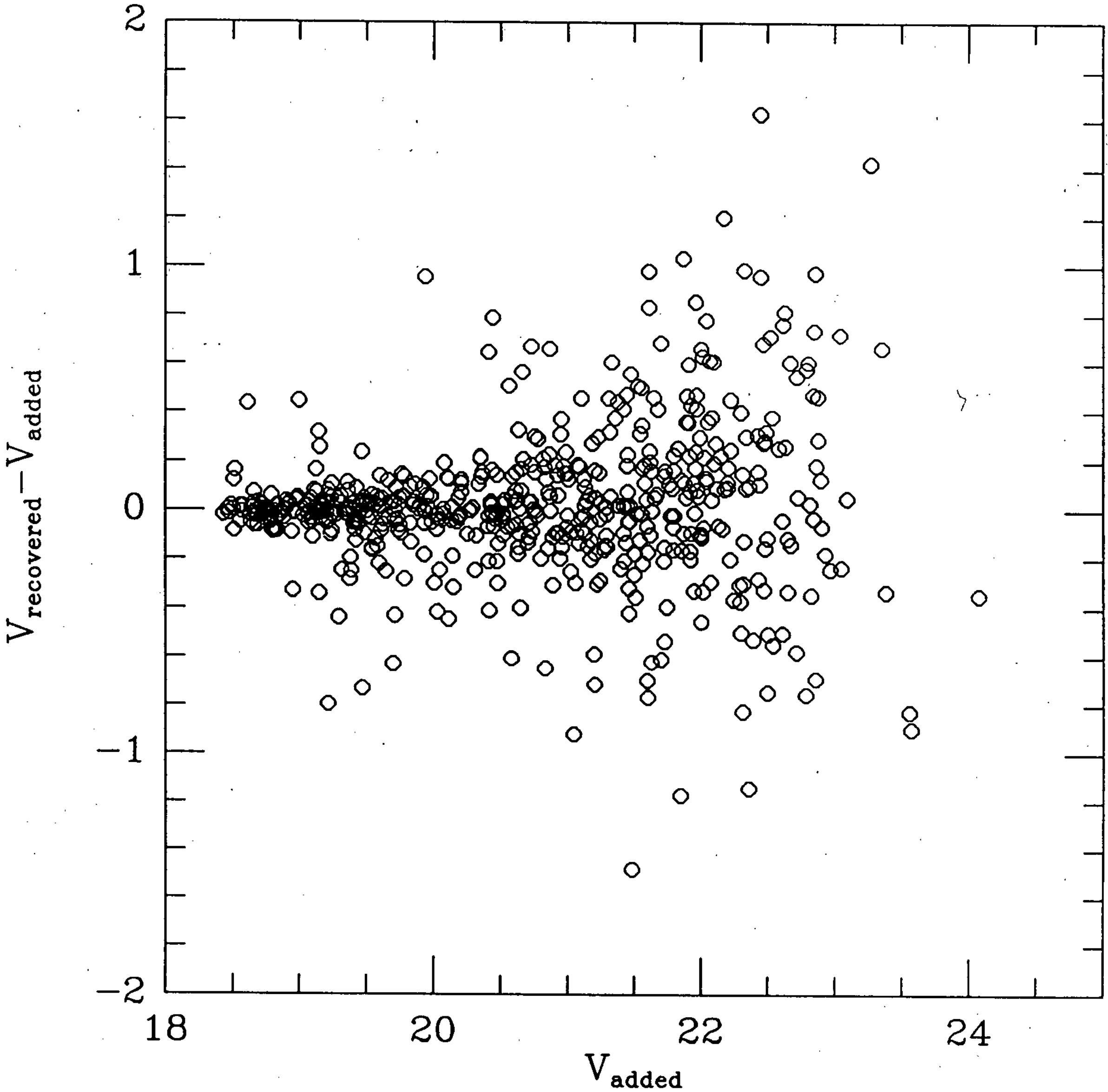

Figure 4.10: RCA2 Inner Field photometric errors from artificial star tests.

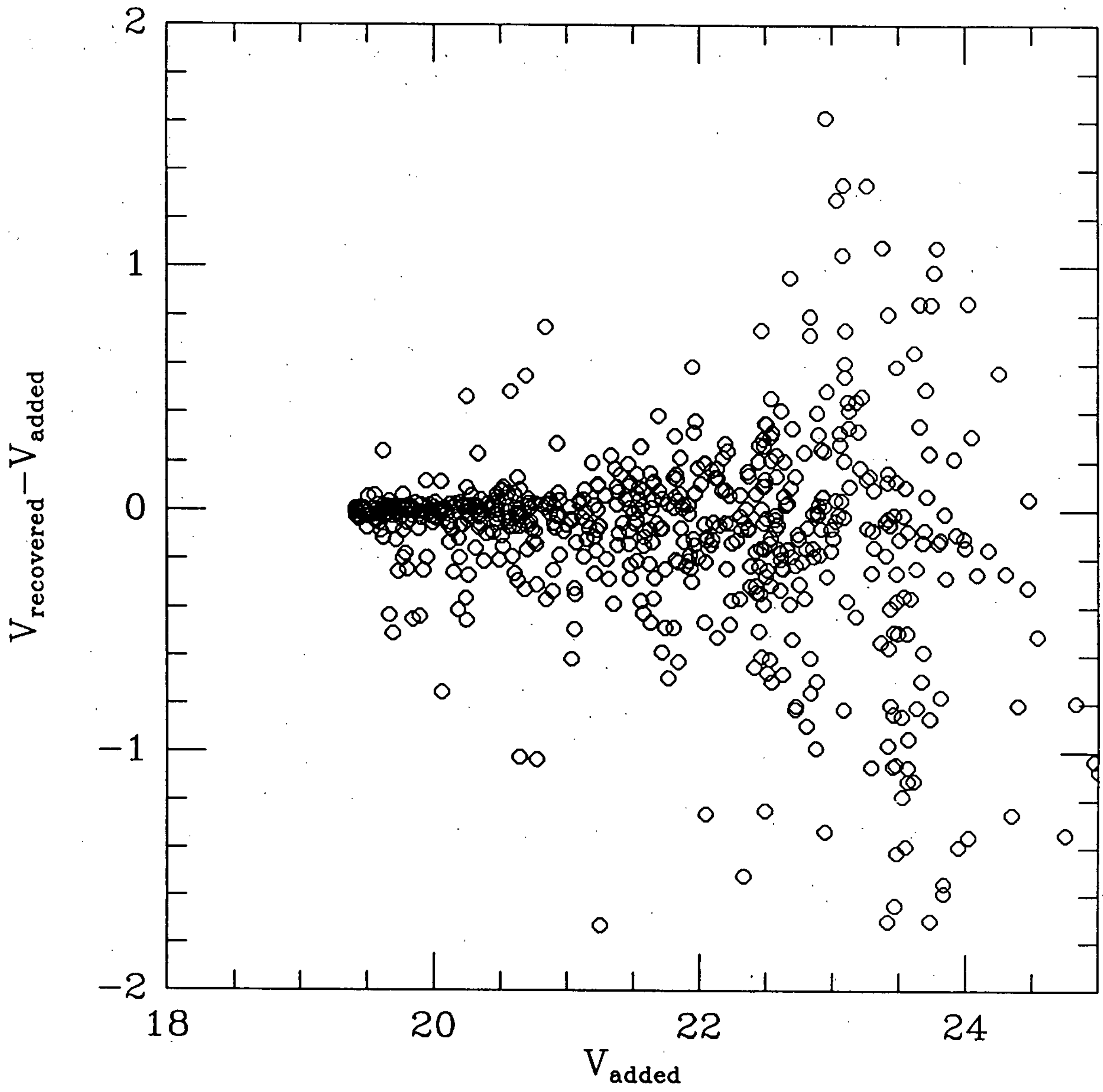

Figure 4.11: RCA2 Outer Field photometric errors from artificial star tests.

Chapter 5

Results

5.1 Photometry

Johnson system photometry in M10 has been carried out by Harris, Racine and deRoux (1976) and Samus and Shugarov (1983). HRdR obtained B and V photometry on many stars observed in this study. Unfortunately HRdR did not obtain photometry in the U band. A V versus $(B-V)$ color-magnitude diagram has been prepared for the stars common to this study and that of HRdR. Figure 5.1 is a color-magnitude diagram for stars in the RCA2 Field measured by HRdR. Figure 5.2 is a color-magnitude diagram for the same stars, as measured in this study, from the RCA2 short-exposure images. The two color-magnitude diagrams agree closely. The scatter in Figure 5.2 appears smaller, as one would expect from CCD versus photographic photometry. Upon closer examination a discrepancy between the V photometry of HRdR and the values determined in this study was noted. Figure 5.3 compares the photometry from this study with that of HRdR. The color transformation is in very good agreement with a difference $< 0^{\mathrm{m}}.005$ in $(B-V)$. However a mean difference of almost $0^{\mathrm{m}}.2$ magnitude exists in V. The source of this rather serious discrepancy may be the shift from Field 2 to RCA2 short exposure photometry; however, a similar plot for the Field 2 data (Figure 5.4) shows a similar offset in V.

It is difficult to account for an error of $0^{\mathrm{m}}.18$ in the CCD photometry. Even though the B and V colors are based on only three standards, a $0^{\mathrm{m}}.18$ shift would be completely inconsistent with the data, as shown in Figures 4.2 and 4.4. Figure 5.3 suggests a linear trend in the transformations, an effect which might arise in the photographic photometry. It is also noteworthy that the photoelectric standards used by HRdR extend only to 16th magnitude, with the exception of one star (Star X) at $V = 18\overset{m}{.}05$. The magnitude of this star is poorly determined. HRdR report $V_{\mathrm{photoelectric}} = 18\overset{m}{.}05$ and $V_{\mathrm{photographic}} = 18\overset{m}{.}34$, while Samus and Shugarov give $V = 18\overset{m}{.}69$. Because of these concerns about the HRdR faint-star photometry, it was decided to adopt the photometric measures from this work and not normalize them to the HRdR magnitude system.

5.2 Deep Color-Magnitude Diagram

The three star lists (Field 2, RCA2, and RCA2 short exposure) were merged and matched to eliminate the possibility of having up to three values for V and $(B-V)$ for each star. The data were then divided into "bright" and "faint" groups. Different criteria were applied to the bright and faint data to select those stars to be plotted in the color-magnitude diagram of Figure 5.5. The selection criteria were:

bright: $\epsilon < 0.008$, $\chi^2 < 2.0$, $12.0 < m_V < 19.0$

faint: $\epsilon < 0.02$, $\chi^2 < 2.0$, $19.0 < m_V < 24.0$

where ϵ is the DAOPHOT photometric error estimator and χ^2 is the DAOPHOT goodness-of-fit parameter. Stars in the range $19.0 < m_V < 24.0$ contained in the RCA2 data were only taken from the outer (less crowded) half of the field. Horizontal-branch stars for the color-magnitude diagram were selected from RCA2 short exposure images and the Inner Field. This is the first color magnitude diagram for M10 which extends more than about 1.0 magnitude below the turnoff. A fiducial sequence for M10 was prepared by fitting a spline to points in Figure 5.5 chosen by eye. The resultant fiducial curve is presented in Figure 5.6 and tabulated in Table 5.1. The horizontal branch stars are tabluated in Table 5.2.

5.2.1 Horizontal Branch

CCDs in general are not particularly effective detectors for exploring the horizontal branch, as their small fields tend to include few bright horizontal branch stars. However, even in this work, enough horizontal branch stars were observed to confirm that M10 has a very blue horizontal branch, extending almost to the luminosity of the turnoff.

In fact, the M10 horizontal branch is so blue that it lies almost entirely blueward of the RR Lyrae gap. Only one RR Lyrae star has been observed in the cluster (Sawyer Hogg, 1973). According to Zinn (1980), the ratio of stars blueward of the RR Lyrae gap to all stars on the horizontal branch is about 0.94.

M10 is a cluster of intermediate metallicity. There are clusters of similar metallicity with much redder horizontal branches. This is a strong indication of a second parameter, other than [Fe/H], which influences the distribution of stars along the horizontal branch. One candidate as suggested by Zinn (1986) is age. The magnitude difference between the horizontal branch and the main sequence turnoff (ΔV_{HB}^{TO}) of a cluster is sensitive to age, while independent of reddening and choice of distance modulus. Post main sequence evolutionary tracks generated by Iben and Rood (1970) demonstrate that stars of different masses will have similar luminosities on the horizontal branch, despite their range in main-sequence luminosity. Hence, as a cluster ages, and the turnoff moves toward fainter (less massive) stars while the horizontal branch stays fairly constant, an increase in ΔV_{HB}^{TO} will result. In the case of very blue horizontal branches, like that of M10, or very red branches, ΔV_{HB}^{TO} may be difficult to determine. Buonanno, *et al.* (1988) find no correlation between ΔV_{HB}^{TO} and $(B-R)/(B+V+R)$ in the 19 clusters they investigated. $(B-R)/(B+V+R)$ is a parameter measuring the blueness of the horizontal branch. B,V and R are, respectively, the number of stars blueward of the RR Lyrae gap, number of variable stars in the gap and number of stars redward of the RR Lyrae gap. $(B-R)/(B+V+R)$ ranges from -1.0 to 1.0, becoming more positive for bluer horizontal branches. However, in an independent treatment of the same data set Zinn to finds indication of an ΔV_{HB}^{TO} versus $(B-R)/(B+V+R)$ corrolation. Unfortunately, ΔV_{HB}^{TO} and other age estimators are often too poorly determined to decide if clusters are coeval or not.

From the data in this study it is unsafe to measure with any confidence the level of the horizontal branch at the RR Lyrae gap,due to the sparseness of the branch there. HRdR estimate the level of the horizontal branch to be $V_{HB} = 14^{m}.65 \pm 0^{m}.05$. However, HRdR have only three or four stars along the horizontal branch and only four or five at the blue edge of the RR-Lyrae gap upon which to base this estimate.

Using $V_{HB} = 14^{m}.65$ from HRdR and estimating the level of the turnoff to be $V_{TO} = 18^{m}.4$ (from this work and that of Samus and Shugarov, 1983), we arrive at $\Delta V_{HB}^{TO} = 3^{m}.75$. In contrast, Buonanno, *et al.* (1988) predict a value of $3^{m}.55$ for a cluster of this metallicity. A similar situation exists with NGC 288. Pound, Janes and Heasley (1987) find $\Delta V_{HB}^{TO} = 3^{m}.73$ for NGC 288.

5.3 Color-Color Diagram and Reddening

Stars of O and B type will be largely free of line-blanketing effects. Hence the colors of such stars should be independent of metallicity. Fortunately, the very blue horizontal branch in M10 contains a large number of very blue bright stars.

By selecting all stars with magnitude $V < 19.0$ on the RCA2 short-exposure B and V frames and the RCA2 U frame, the $(U-B)$ versus $(B-V)$ diagram shown in Figure 5.7 was constructed. By comparing this color-color diagram to the dereddened Hyades main sequence from Sandage (1969), the reddening was measured to be $\mathrm{E}(B-V) = 0.273 \pm 0.034$, as shown in Figure 5.8. This estimate of $\mathrm{E}(B-V)$ assumes a reddening vector of 0.733, appropriate for O and B-type stars (Mihalas and Binney, 1981, p.186).

5.4 Metallicity

Because the main sequence contains stars later than type B, the shape of the main sequence in the $(U-B)$ versus $(B-V)$ plane will change as line blanketing becomes more pronounced. Hence, the shape of the color-color sequence depends on cluster metallicity. A relationship has been established between metallicity and $\delta(U-B)_{0.6}$ (Richer and Fahlman, 1986), where $\delta(U-B)_{0.6}$ is the difference in $(U-B)$ between the Hyades main sequence and the cluster main sequence at $(B-V)_\circ = 0.6$. Sandage (1969) has tabulated a series of factors to normalize $\delta(U-B)$ measured at other $(B-V)$ colors to $(B-V)_\circ = 0.6$. This makes it possible to determine $\delta(U-B)_{0.6}$ even if $\delta(U-B)$ is measured at any of several other $(B-V)$ colors.

The dereddened color-color diagram for M10 (Figure 5.9) is richly populated in the range $0.3 < (B-V)_\circ < 0.7$. Measurements of $\delta(U-B)$ were obtained at a series of intervals in this range and corrected to $\delta(U-B)_{0.6}$. The results are given in Table 5.3 and the data is shown in Figure 5.9. An average value of $\delta(U-B)_{0.6} = 0.213 \pm 0.011$ was found. It should be noted that a reddening vector of slope, $\mathrm{E}(U-B)/\mathrm{E}(B-V) = 0.8$ was used in preparing the dereddened color-color diagram, as adopted in Fahlman, Richer and VandenBerg (1985).

Richer and Fahlman (1986), have tabulated [Fe/H] versus $\delta(U-B)_{0.6}$ for nine clusters. Table 5.4 and Figure 5.10 are reproduced from Richer and Fahlman (1986). In this work, a quadratic curve has been fitted through the data points in Figure 5.10

(excluding the two outliers of intermediate metallicity, M3 and NGC6752). By using the value for $\delta(U-B)_{0.6}$ derived above and the relationship illustrated in Figure 5.10, the metallicity of M10 was found to be [Fe/H] $= -1.54 \pm 0.20$. In light of the wide scatter about the curve in the intermediate metallicity region, this formal error may well be an underestimate of the real uncertainty. An error range of twice this size may be more realistic.

5.5 Distance Modulus

The best way to determine the distance to a globular cluster is to compare its main sequence in a color-magnitude diagram to a main sequence of field subdwarfs. There is a small sample of subdwarfs with reasonably accurate parallax measurments. Lutz, Hanson and van Altena (1987), using a sample of 50 subdwarfs with well established trigonometric parallaxes and spectroscopic [Fe/H] determinations, have developed a formula which gives a subdwarf fiducial if the metallicity is known[1]. Given the reddening and metallicity , one determines a distance modulus simply by shifting this subdwarf fiducial to match the cluster main sequence. A subdwarf fiducial was prepared for the reddening and metallicity derived in §5.3 and §5.4, $E(B-V) = 0.273$ and [Fe/H] $= -1.54$. A distance modulus of $(m-M)_V = 14^{m}.4 \pm 0^{m}.2$ yields the best match between the cluster main sequence and this subdwarf fiducial. This modulus will be adopted for the remainder of this discussion. The subdwarf fiducial is shown in Figure 5.11, along with the M10 color-magnitude diagram.

This estimate of distance with HRdR's estimate of the horizontal branch level ($V = 14.65$) combine to give an exceptionally bright horizontal branch level of $M_V(HB) = 0^{m}.25$. Any estimate of the M10 horizontal branch level should be regarded as rather uncertain, and not necessarily representative of normal horizontal branchs. The sparseness of the horizontal branch in the region of the RR Lyrae gap, and the lack of RR Lyrae stars, tends to make the level of the horizontal branch very uncertain. Also the horizontal branch of M10 is hardly normal, so it may be hasty to assume that the horizontal branch of this cluster, and other very blue horizontal branch clusters, should be similar to those of other clusters.

[1] $M_V = 1.41 + 5.17(B-V) - 0.94$[Fe/H]

5.6 Age

By comparing a set of theoretical isochrones (VandenBerg and Bell, 1985 1985) to the M10 fiducial the age of M10 was estimated. Isochrones are available for [Fe/H] = -1.27 with Y = 0.20, Z = 0.0010, $\alpha = 1.6$, and [Fe/H] = -1.77 with Y = 0.20, Z = 0.0003, $\alpha = 1.6$, both significantly different from that for M10, [Fe/H] = -1.54. Therefore a set of isochrones was calculated by interpolation between [Fe/H] = -1.27 and [Fe/H] = -1.77 at [Fe/H] = -1.54. The resulting isochrones with [Fe/H] = -1.54 should also have, Y = 0.20, Z = 0.0005, $\alpha = 1.6$. The isochrones used for the interpolation were not oxygen-enhanced.

The interpolated isochrone was generated only over the magnitude region covered by both the known isochrones. The known isochrones were broken into an equal number of steps. At each step $(B-V)$ and M_V were determined for the new isochrone, by interpolating linearly on [Fe/H] between the input isochrones. Comparison to the interpolated isochrone should be superior to comparison to a set of isochrones removed from the appropriate metallicity by a few tenths of a dex.

The interpolated isochrones were then reddened by E$(B-V) = 0.273$ and shifted by $(\mathrm{m}-\mathrm{M})_V = 14.4$ to match M10. These isochrones are shown against the M10 color-magnitude diagram in Figure 5.12. The match was improved by further shifting the isochrones by $0^{\mathrm{m}}.04$ redward in color. A similar effect has been observed by other researchers and is attributed to the lack of a simple correlation between $(B-V)$ and T_{eff}. Gratton and Ortolani (1988) discuss this point. An age of 17 ± 1 Gyr was estimated.

The effects of errors in observational quantities on cluster age as determined by isochrone fitting has recently been discussed by Bolte (1989a). An error in distance modulus of $0^{\mathrm{m}}.15$ or error in metallicity of 0.25 dex, can alter the age of the cluster by 2 Gyr. An error in reddening of $0^{\mathrm{m}}.03$ can also incure a 2 Gyr error in age. This empasizes the risk in comparing ages of clusters determined by different methods, or even comparing ages of clusters whose observational parameters were determined differently.

Recently Bolte (1989b) produced a deep color-magnitude diagram for NGC 288. NGC 288 and M10 are of similar metallicity and horizontal branch morphology (Tables 2.1 and 2.2). Figure 5.13 shows the M10 fiducial described above and the NGC 288 fiducial due to Bolte overlaid. The M10 fiducial has been dereddened and converted to

M_V using the reddening and distance modulus described in §5.3 and §5.5. in this work. The NGC 288 fiducial has been dereddened and converted to M_V using the reddening and distance modulus adopted by Bolte (1989b). Also shown in Figure 5.13 are a set of isochrones for [Fe/H] = −1.54 , and ages of 14, 16 and 18 Gyr, described above. The isochrones have been shifted by $0\overset{m}{.}04$ in color to improve the fit. The two fiducials are in excellent agreement along the main sequence and are in close agreement around the turnoff and along the subgiant branch. The agreement between the isochrones suggests that M10 and NGC 288 are coeval to within 2.0 Gyr.

5.7 Luminosity Functions

Luminosity functions were derived for the Inner Field, the RCA2 Inner Field and RCA2 Outer Field. Bin jumping was not directly addressed. A test was made to evaluate how severely it affected the results. A matrix was created where each element represented the number of stars added, and recovered at a given magnitude bin, as in Drukier, *et al.* (1988). When the derived luminosity functions were multiplied by the normalized matrix, the result closely matched the observed distribution of stars. The recovered stars for the derived luminosity functions were taken to be those which departed from the magnitude they were added at by less then 0.5 magnitudes.

The luminosity functions are tabulated and illustrated in Tables 5.5, 5.6, 5.7, and Figures 5.14, 5.15, 5.16. The three luminosity functions are overlaid in Figure 5.17. The luminosity functions are truncated at the faint end when the completeness falls below 30%, and at the bright end when the number of stars in each bin falls below ten.

The leveling off of the Inner Field luminosity function in its last four bins could be interpreted as an indication of mass segregation. Taking this as firm evidence of mass segregation would be hasty, however the trend is correct.

5.8 Mass Function

Stellar magnitudes were converted to mass using a VandenBerg and Bell (1985) isochrone for [Fe/H] = −1.77 and age of 18 Gyr. For [Fe/H] = −1.27,−1.77 and ages of 16 or 18 Gyr, plots of M_V versus mass showed little variation at the faint end. Horizontal branch stars were excluded from the mass functions, this only affected the high mass end of the Inner Field mass function. Stars in the range $V = 16$ to

$18^{m}.5$ were all assigned to a bin with mass 0.800 $M_{\odot}$. The mass functions are presented in Figure 5.18 and indicate an apparent mass function index of $x_{app} \simeq 0.5$, for a mass function of the form $\Phi(m)\,dm = m^{-(1+x)}\,dm$. At masses below 0.5$M_{\odot}$ a rapid upturn in the mass function of M13 (from $x_{app} \simeq 0.0$ to $x_{app} \simeq 3.0$) has been observed by Drukier, *et al.* (1988). The data in this study barely extend to 0.5$M_{\odot}$ and show no evidence of sudden upturn. Despite being well fit by a single mass function index, it may be unwise to extrapolate this index to less massive stars.

5.9 King Models

Multi-mass King models for M10 were generated for global mass indices of $x_{global} = -0.5$ to 2.0. The masses used ranged from 0.1$M_{\odot}$ to 0.8$M_{\odot}$ in 7 bins; in addition, two bins represented white dwarfs. The models do not allow for velocity anisotropy. A plot of apparent mass function index versus cluster radius for these models is given in Figure 5.19. From this figure, the best estimate of the global mass function of M10 is $x_{global} = 0.5 \pm 0.5$. The thick horizontal error bar in Figure 5.19 represents the radius over which the RCA2 observations were made, and the thin horizontal line represents the radius spaned by the Inner Field. In this region one would expect to observe a change in x_{app} of ~ 0.4 for $0.0 \leq x_{global} \leq 1.0$, roughly the estimated uncertainty in x_{app}. Hence one would not expect to observe strong mass segregation over this region in the cluster.

This estimate agrees with the relationship between metallicity and mass function index reported by Pryor, Smith and McClure (1986). Their data are reproduced in Table 5.8, and plotted in Figure 5.20, where M10 has been included.

$(B-V)$	V
1.06	14.50
1.05	14.75
1.03	15.00
1.02	15.25
1.00	15.50
0.99	15.75
0.97	16.00
0.95	16.25
0.94	16.50
0.92	16.75
0.92	17.00
0.90	17.25
0.89	17.50
0.85	17.75
0.74	18.00
0.70	18.25
0.69	18.50
0.70	18.75
0.72	19.00
0.74	19.25
0.76	19.50
0.78	19.75
0.82	20.00
0.87	20.25
0.92	20.50
0.99	20.75
1.04	21.00

Table 5.1: M10 Fiducial.

RCA2 Short Exposure			Inner Field	
$(B-V)$	V	$(U-B)$	$(B-V)$	V
0.053	18.092	−0.445	0.159	16.620
0.072	18.210	−0.553	0.161	16.977
0.082	17.174	−0.398	0.184	16.032
0.118	16.310	−0.249	0.202	16.370
0.126	17.259	−0.503	0.218	16.281
0.127	17.000	−0.318	0.234	16.144
0.145	16.210	−0.182	0.258	15.390
0.149	16.207	−0.268	0.260	15.275
0.150	16.163	−0.234	0.287	14.960
0.152	16.488	−0.255	0.296	14.891
0.165	16.169	−0.143	0.309	13.980
0.181	16.854	−0.344	0.374	14.870
0.210	15.847	−0.031	0.425	14.698
0.217	15.123	−0.021	0.489	14.635
0.218	15.469	0.090		
0.219	15.485	0.028		
0.222	15.642	0.017		
0.225	15.829	−0.080		
0.275	15.087	0.149		
0.283	17.650	0.194		
0.312	15.135	0.160		

Table 5.2: M10 horizontal branch stars found in the Inner Field and RCA2 short exposure data.

(B−V)$_\circ$	$\delta(U-B)$	$\frac{\delta(U-B)_{0.6}}{\delta(U-B)}$	$\delta(U-B)_{0.6}$
0.35	0.207	1.23	0.255
0.40	0.172	1.20	0.206
0.45	0.166	1.18	0.196
0.50	0.223	1.10	0.245
0.55	0.212	1.01	0.214
0.60	0.180	1.00	0.180
0.65	0.198	1.00	0.198
		average $\delta(U-B)_{0.6}$ =	0.213
		mean of mean =	0.011

Table 5.3: Ultraviolet excess determination. $\delta(U-B)$ was measured in bins 0.05 wide in $(B-V)$ color centered at the colors in column one. $\delta(U-B)$ was converted to $\delta(U-B)_{0.6}$ using correction factors from Sandage(1969) in column 3.

cluster	[Fe/H]	$\delta(U-B)_{0.6}$	Source of $\delta(U-B)_{0.6}$
47 Tuc	−0.59	0.09	(1)
M71	−0.60	0.10	(2)
M4	−0.72	0.13	(3)
NGC 6752	−1.35	0.22	(4)
M3	−1.47	0.17	(5)
M13	−1.47	0.21	(6)
M5	−1.49	0.21	(7)
M92	−2.01	0.24	(5)
M15	−2.21	0.25	(8)

Table 5.4: Metallicity and ultraviolet excess for some galactic globulars. Reproduced from Richer and Fahlman (1986). Sources of data are: (1) Hesser and Hartwick (1977), (2) Arp and Hartwick (1971), (3) Richer and Fahlman (1984), (4) Carney (1979), (5) Sandage (1970), (6) Richer and Fahlman (1986), (7) Arp (1962), (8) Fahlman, Richer and VandenBerg (1985).

M_V	V	mass ($M_\odot$)	n_{obs}	n_{add}	n_{rec}	n_{field}	n_{HB}	%	$\%_{err}$	Φ
1.85	16.25	0.800	15	55	24	1.0	4	44	56	24.7
2.35	16.75	0.800	14	85	40	1.0	2	47	60	20.1
2.85	17.25	0.800	16	76	29	2.7	0	38	34	39.2
3.35	17.75	0.800	54	106	46	2.7	0	43	19	121.7
3.85	18.25	0.800	99	123	46	2.7	0	37	16	262.0
4.35	18.75	0.778	132	97	49	2.7	0	51	14	258.6
4.85	19.25	0.757	147	76	34	8.2	0	45	18	320.4
5.35	19.75	0.724	98	81	28	8.2	0	35	21	275.3

Table 5.5: Inner field artificial star tests. Mass is from VandenBerg and Bell (1985) isochrones. n_{field} is the expected number of field stars from Ratnatunga and Bachall (1985). n_{HB} is the number horizontal branch stars identified. % is the fraction of added stars recovered, expressed as a percentage. $\%_{err}$ is the fractional error in the recovery fraction, expressed as a percentage. Φ is the derived luminosity function.

M_V	V	mass ($M_\odot$)	n_{obs}	n_{add}	n_{rec}	n_{field}	%	$\%_{err}$	Φ
2.85	17.25	0.800	14	0	0	4.5	100	41	9.5
3.35	17.75	0.800	40	0	0	4.5	100	18	35.5
3.85	18.25	0.800	67	0	0	4.5	100	13	62.5
4.35	18.75	0.778	116	71	68	4.5	96	14	116.6
4.85	19.25	0.757	163	86	78	13.7	91	18	166.6
5.35	19.75	0.724	173	79	63	13.7	80	17	203.3
5.85	20.25	0.691	202	72	55	13.7	76	16	250.8
6.35	20.75	0.653	178	98	64	13.7	65	16	258.9
6.85	21.25	0.622	174	113	67	22.8	59	19	270.7
7.35	21.75	0.574	118	132	65	22.8	49	22	216.9
7.85	22.25	0.531	90	139	46	22.8	33	24	249.2

Table 5.6: RCA2 Inner Field artificial star tests. Mass is from VandenBerg and Bell (1985) isochrones. n_{field} is the expected number of field stars from Ratnatunga and Bachall (1985). % is the fraction of added stars recovered, expressed as a percentage. $\%_{err}$ is the fractional error in the recovery fraction, expressed as a percentage. Φ is the derived luminosity function. There were no horizontal branch stars identified over the magnitudes tabulated.

M_V	V	mass ($M_\odot$)	n_{obs}	n_{add}	n_{rec}	n_{field}	%	$\%_{err}$	Φ
3.35	17.75	0.800	13	0	0	4.5	100	45	8.5
3.85	18.25	0.700	32	0	0	4.5	100	21	27.5
4.35	18.75	0.778	47	0	0	4.5	100	16	42.5
4.85	19.25	0.757	64	17	17	13.7	100	17	50.3
5.35	19.75	0.724	96	94	88	13.7	94	24	88.9
5.85	20.25	0.691	94	87	74	13.7	85	24	96.9
6.35	20.75	0.653	114	78	69	13.7	88	21	115.2
6.85	21.25	0.622	95	69	51	22.8	74	30	105.8
7.35	21.75	0.574	108	94	70	22.8	74	27	122.3
7.85	22.25	0.531	84	108	61	22.8	56	28	126.0
8.35	22.75	0.417	89	177	62	22.8	35	23	231.3

Table 5.7: RCA2 Outer Field artificial star tests. Mass is from VandenBerg and Bell (1985) isochrones. n_{field} is the expected number of field stars from Ratnatunga and Bachall (1985). % is the fraction of added stars recovered, expressed as a percentage. $\%_{err}$ is the fractional error in the recovery fraction, expressed as a percentage. Φ is the derived luminosity function. There were no horizontal branch stars identified over the magnitudes tabulated.

Cluster	[Fe/H]	x_{global}
M15	−2.05	1.4
M68	−1.96	1.0
M13	−1.58	0.7
M3	−1.51	0.8
NGC 6752	−1.50	0.6
M5	−1.38	0.7
M4	−1.22	−0.7
47 Tuc	−0.79	−0.8

Table 5.8: Metallicity versus global mass function exponent relationship. From Pryor, Smith and McClure (1986).

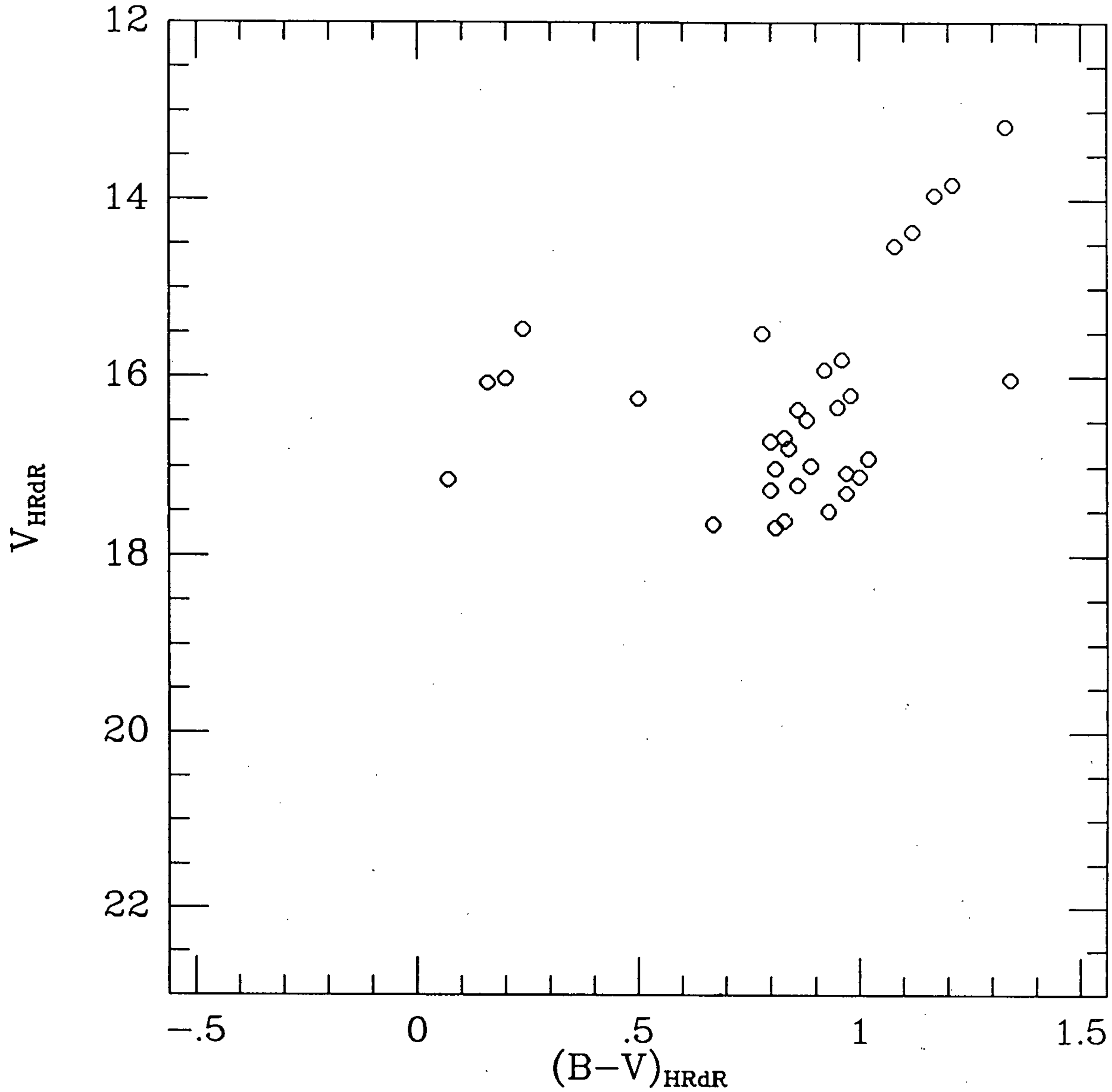

Figure 5.1: Harris, Racine and deRoux (1976) photometry for stars in the RCA2 Field. Figure 5.2 is a similar diagram using the photometry from this study.

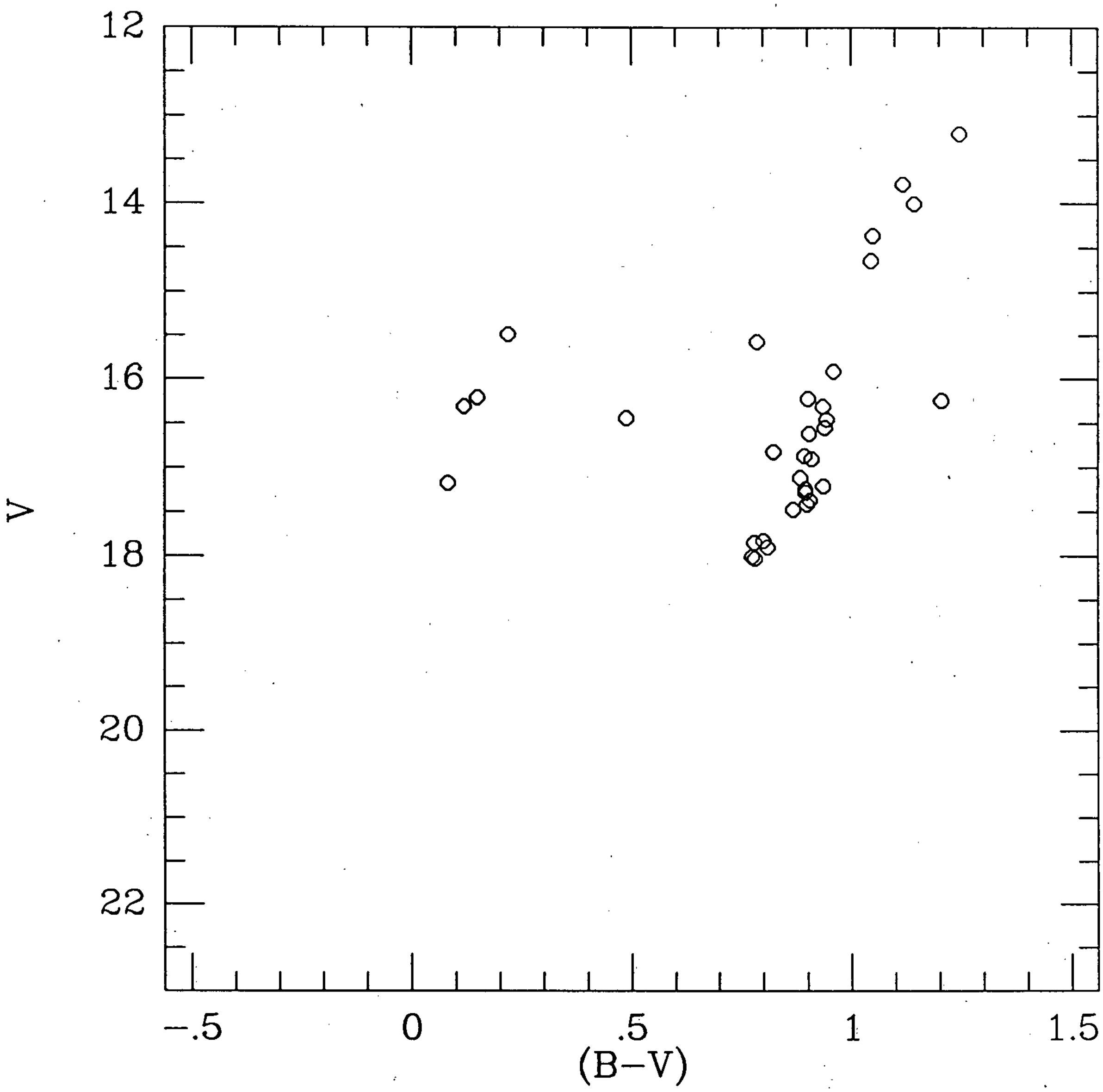

Figure 5.2: RCA2 short exposure photometry for stars in Figure 5.1 .

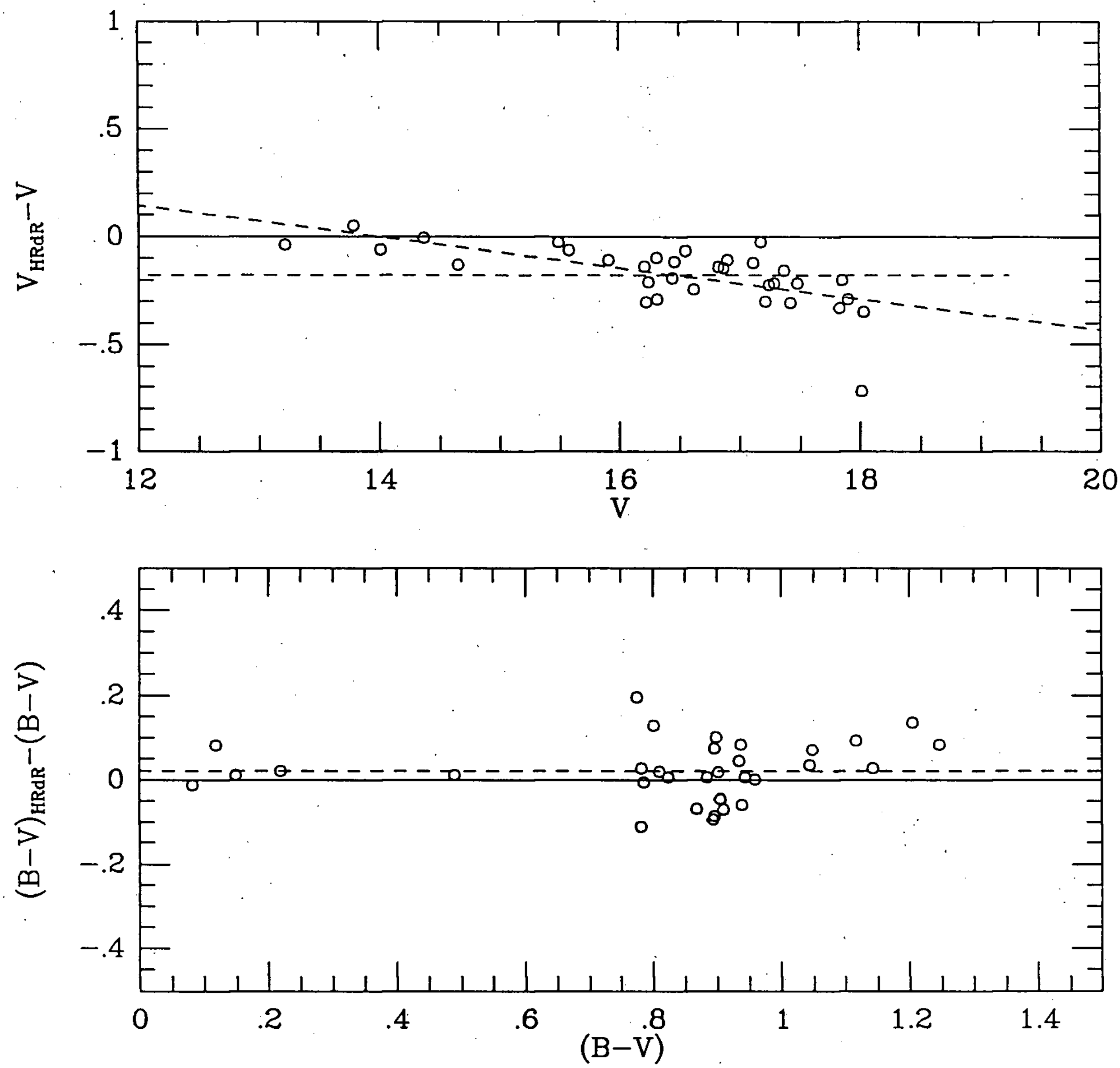

Figure 5.3: RCA2 short exposure photometry compared to Harris Racine and deRoux (1976) photometry. Horizontal dashed lines represent offsets of 0.021 and −0.18 in color and magnitude, respectivly. The sloping dashed line in the upper panel is a best least squares fit to the data, with a slope of −0.072.

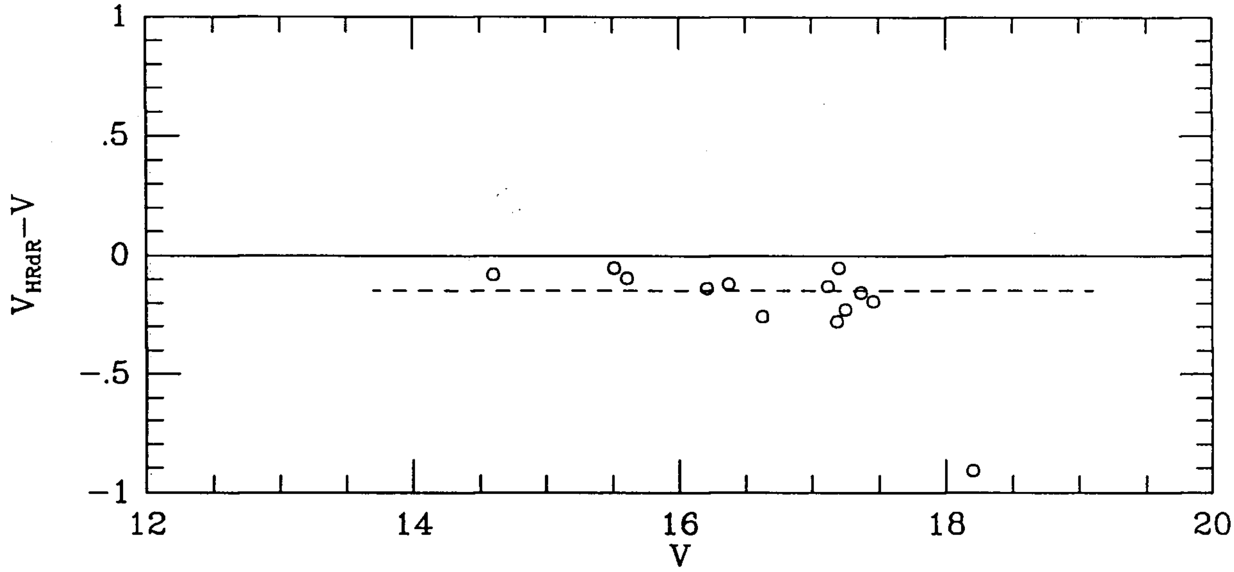

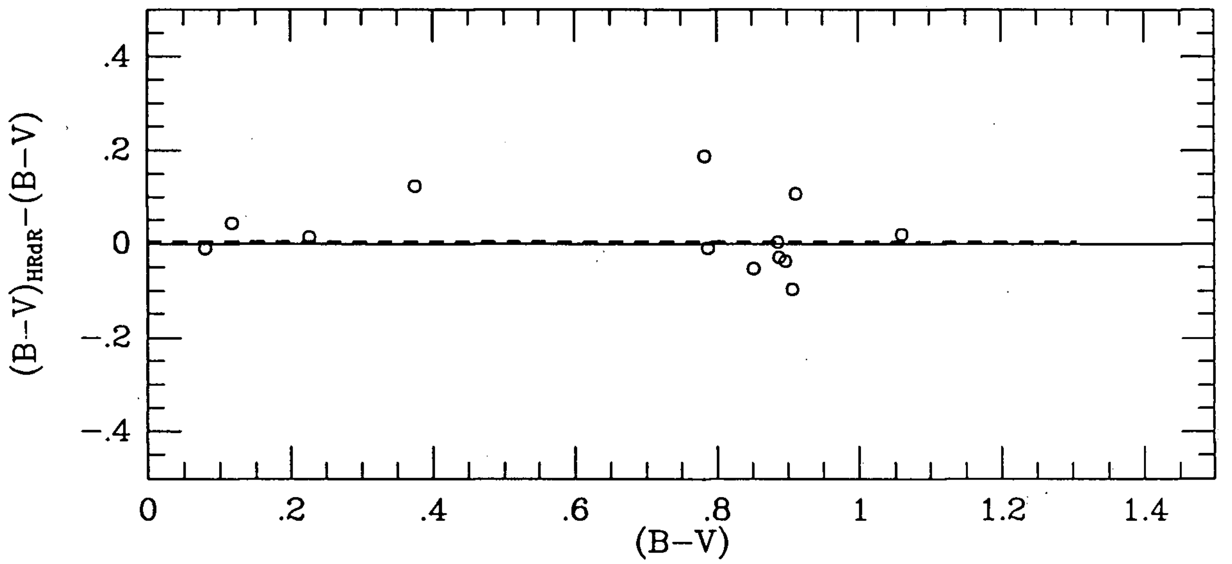

Figure 5.4: Field 2 photometry compared to Harris Racine and deRoux (1976) photometry. Horizontal dashed lines represent offsets of +0.005 and −0.15 in color and magnitude, respectively.

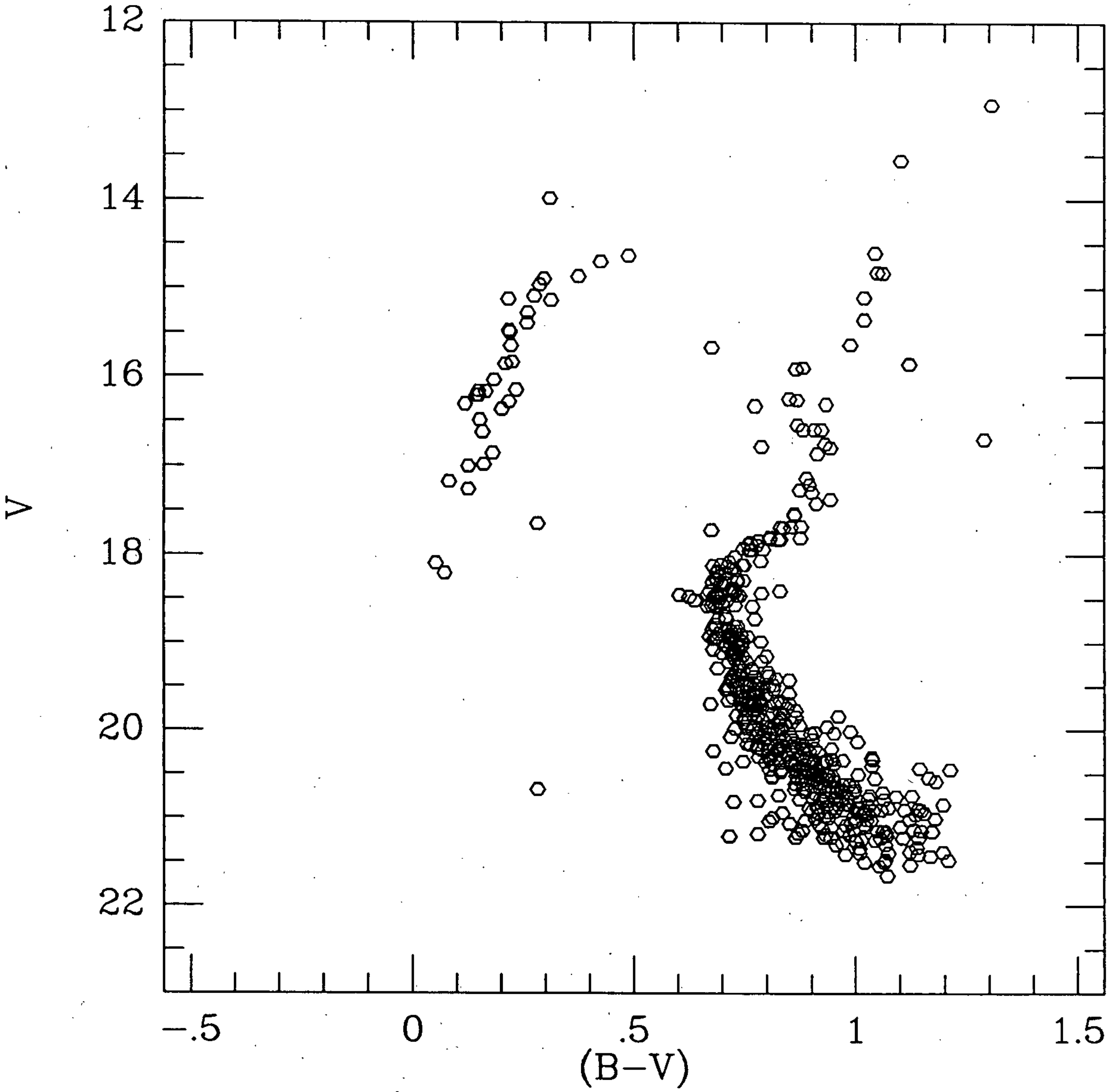

Figure 5.5: Color magnitude diagram for combined Inner Field, Field 2, RCA2, and RCA2 short exposure data.

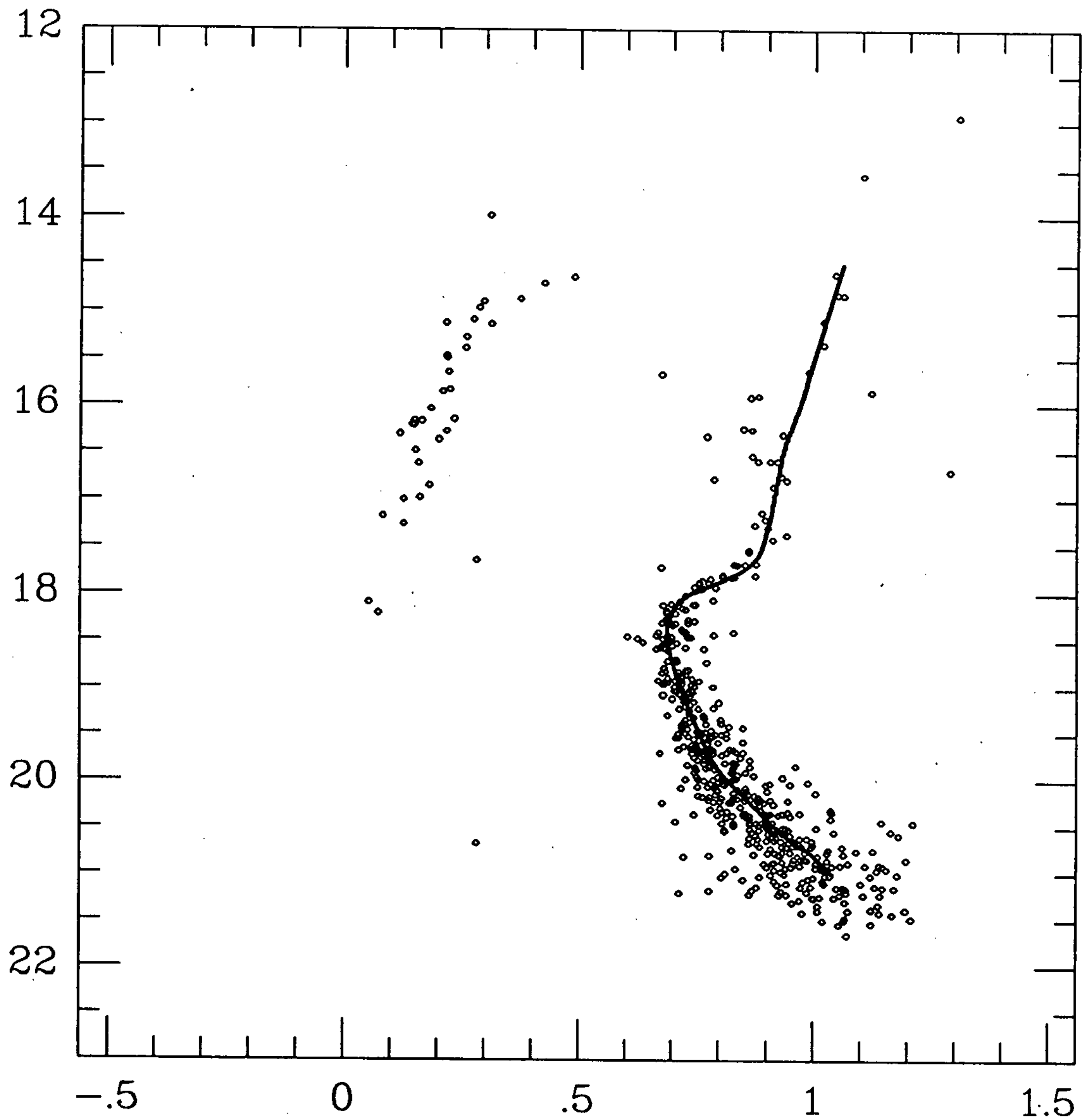

Figure 5.6: M10 fiducial overlaid on the M10 color-magnitude diagram.

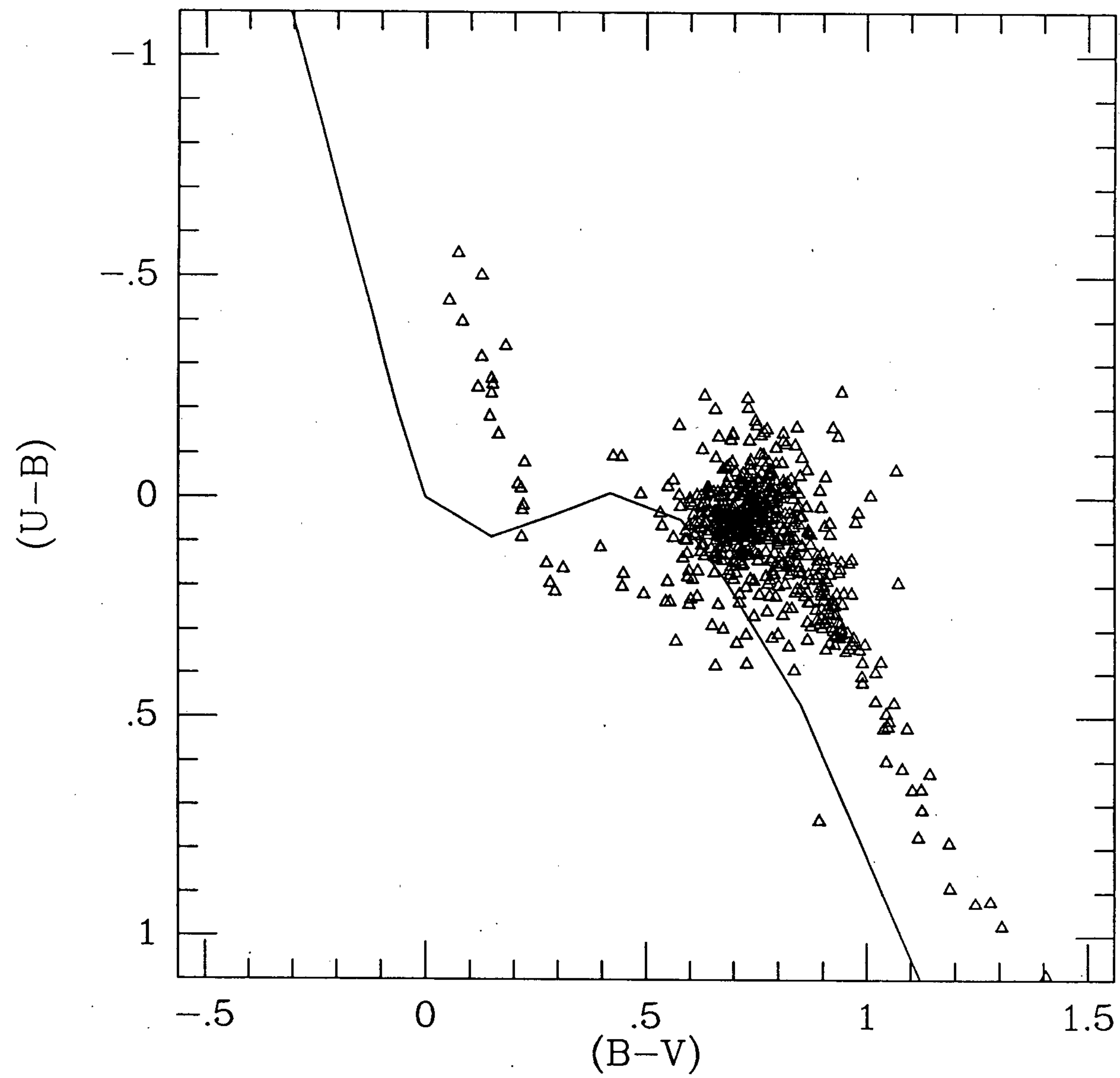

Figure 5.7: Color-color diagram. The data is taken from RCA2 short exposure frames, and only stars with $V < 19.0$ shown. The line represents the Population I main sequence (Mihalas and Binney, 1981, Table 3-3).

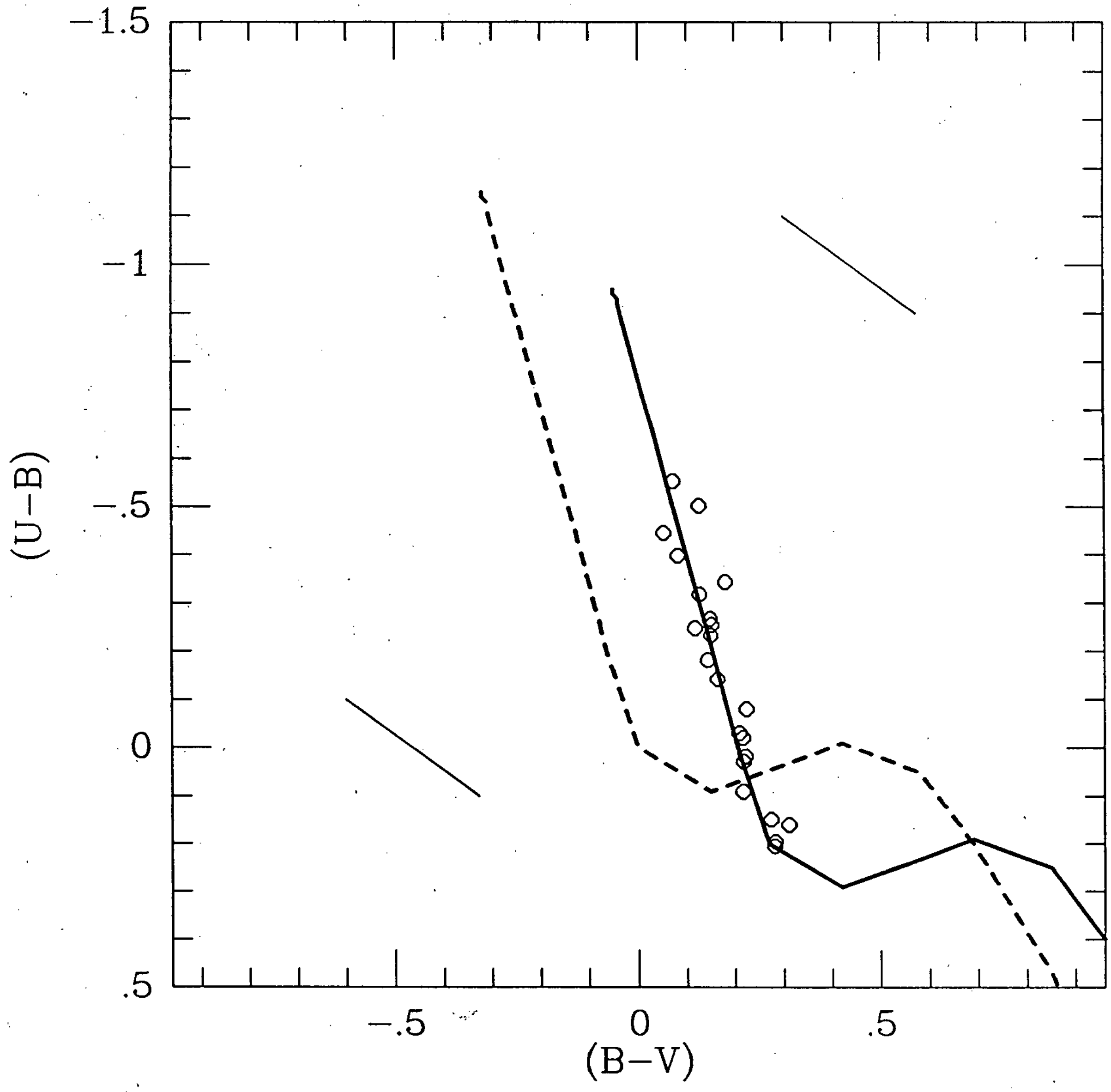

Figure 5.8: Reddening in M10. The dashed line is the Population I main sequence (Mihalas and Binney, 1981, Table 3-3), the solid line is the Population I main sequence with E$(B-V)$ $= 0.273$ and E$(U-B)$ $= 0.200$. The error in the fit is 0.034. The lines to the upper right and lower left are sample reddening vectors.

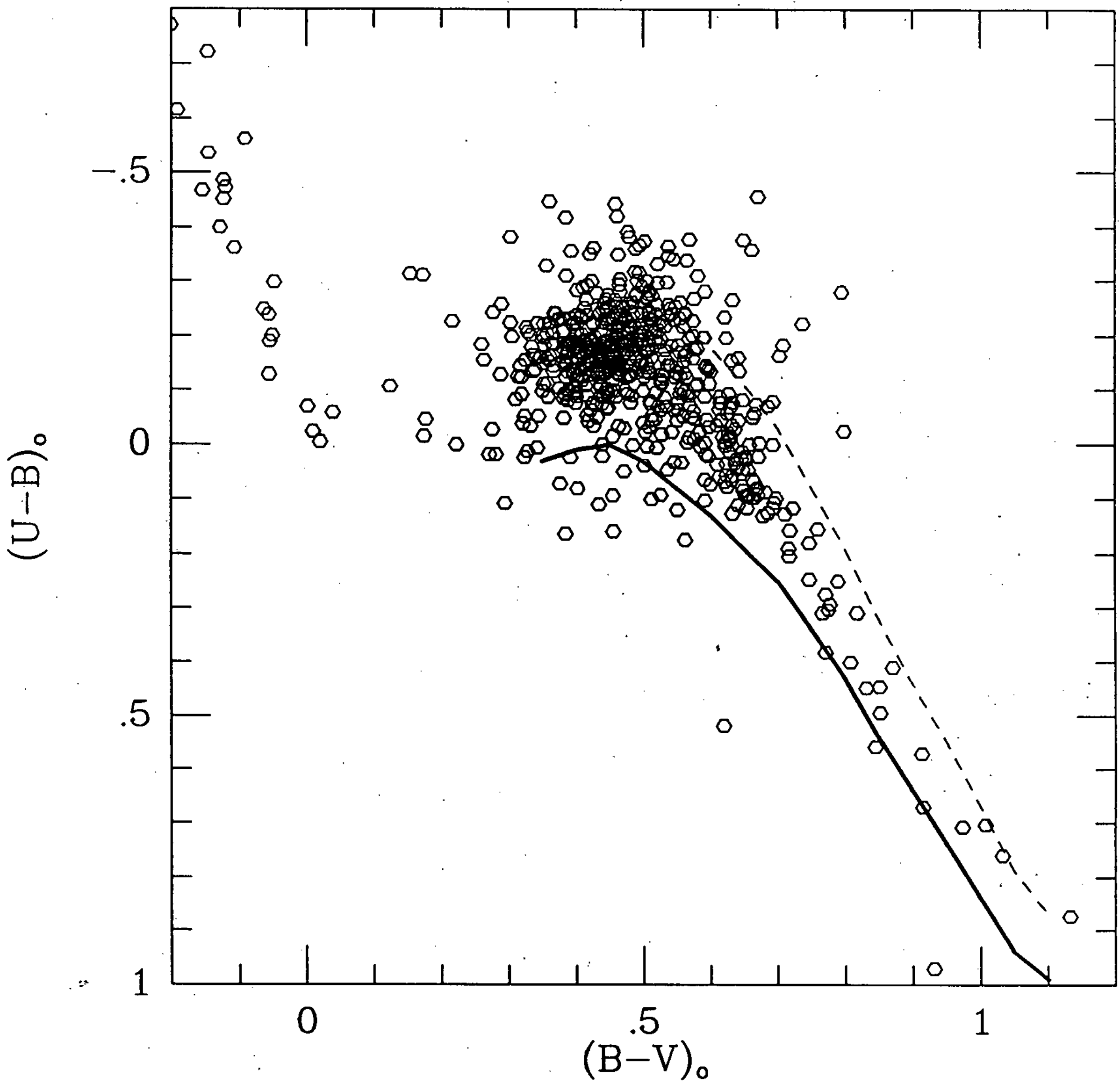

Figure 5.9: Dereddened color-color diagram of M10. The solid curve is the Hyades sequence (Sandage, 1969) and the dashed line is the zero metallicity relationship.

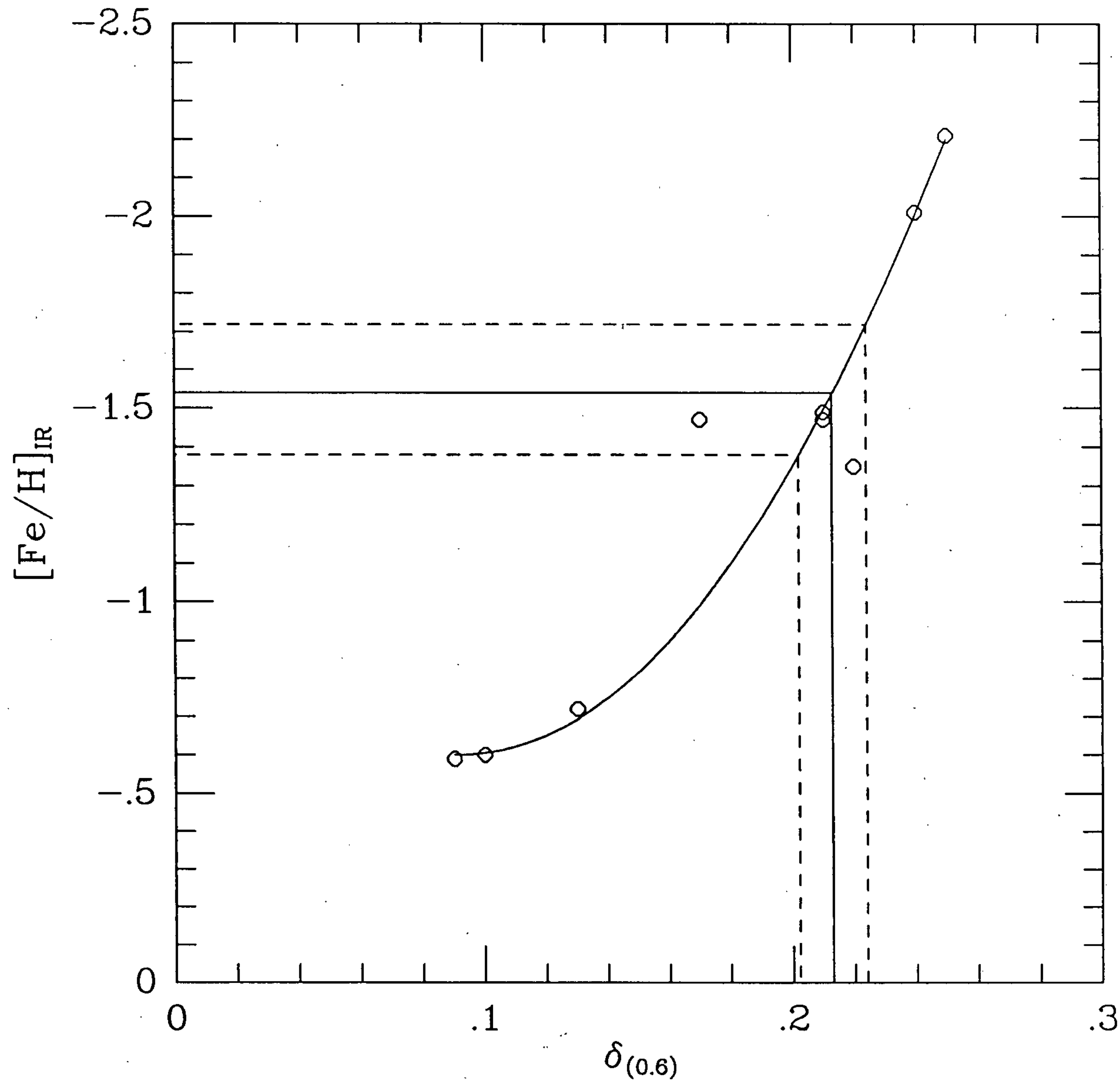

Figure 5.10: Metallicity determination. Solid straight lines correspond to $\delta(U-B)_{0.6} = 0.213 \pm 0.011$ and [Fe/H] $= -1.54$. Dashed lines are error estimators.

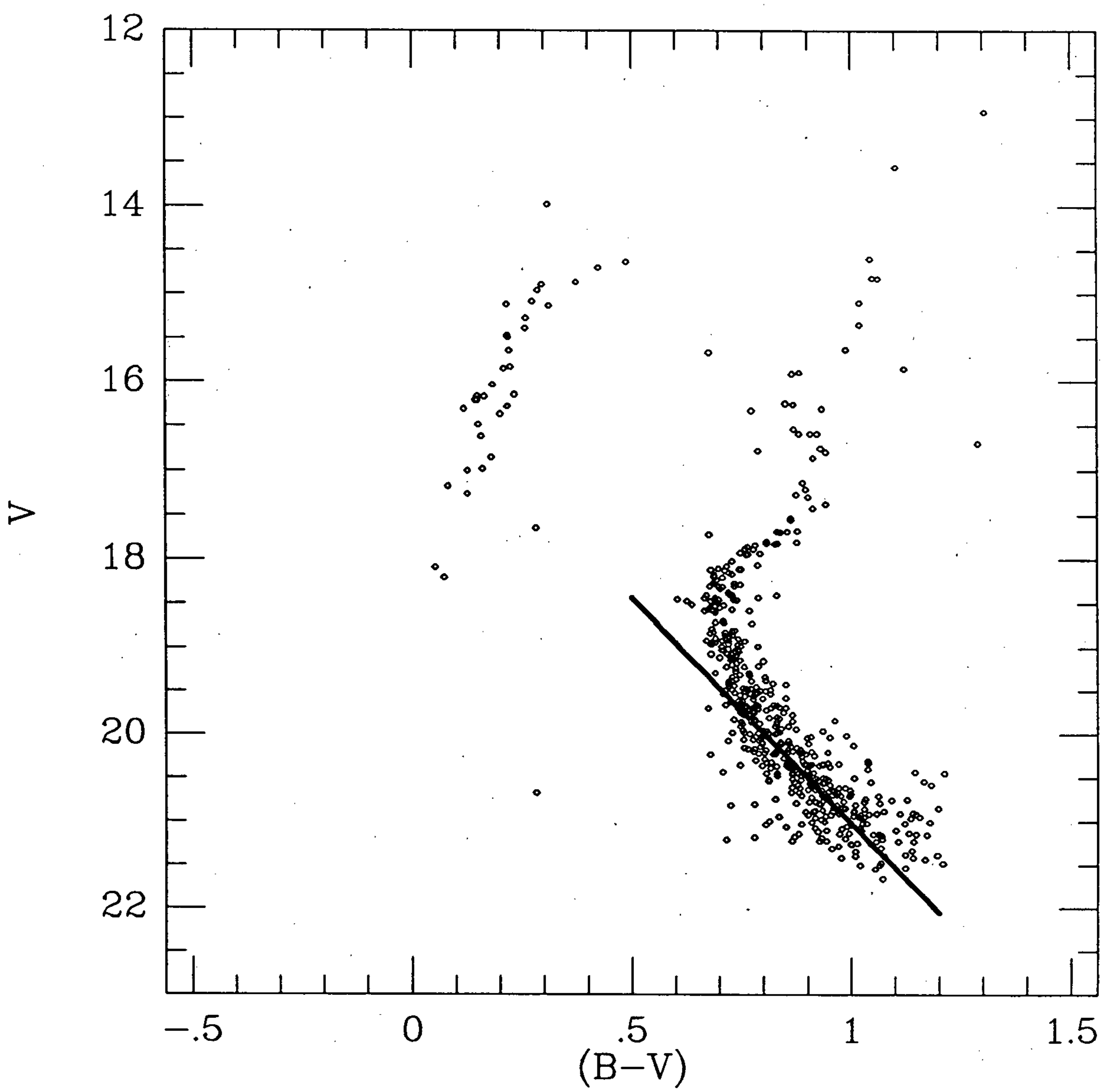

Figure 5.11: Field subdwarf fiducial for [Fe/H] = −1.54 overlaid on the M10 color-magnitude diagram. The subdwarf fiducial has been shifted by $(\mathrm{m}-\mathrm{M})_V = 14.4$, and $\mathrm{E}(B-V) = 0.273$.

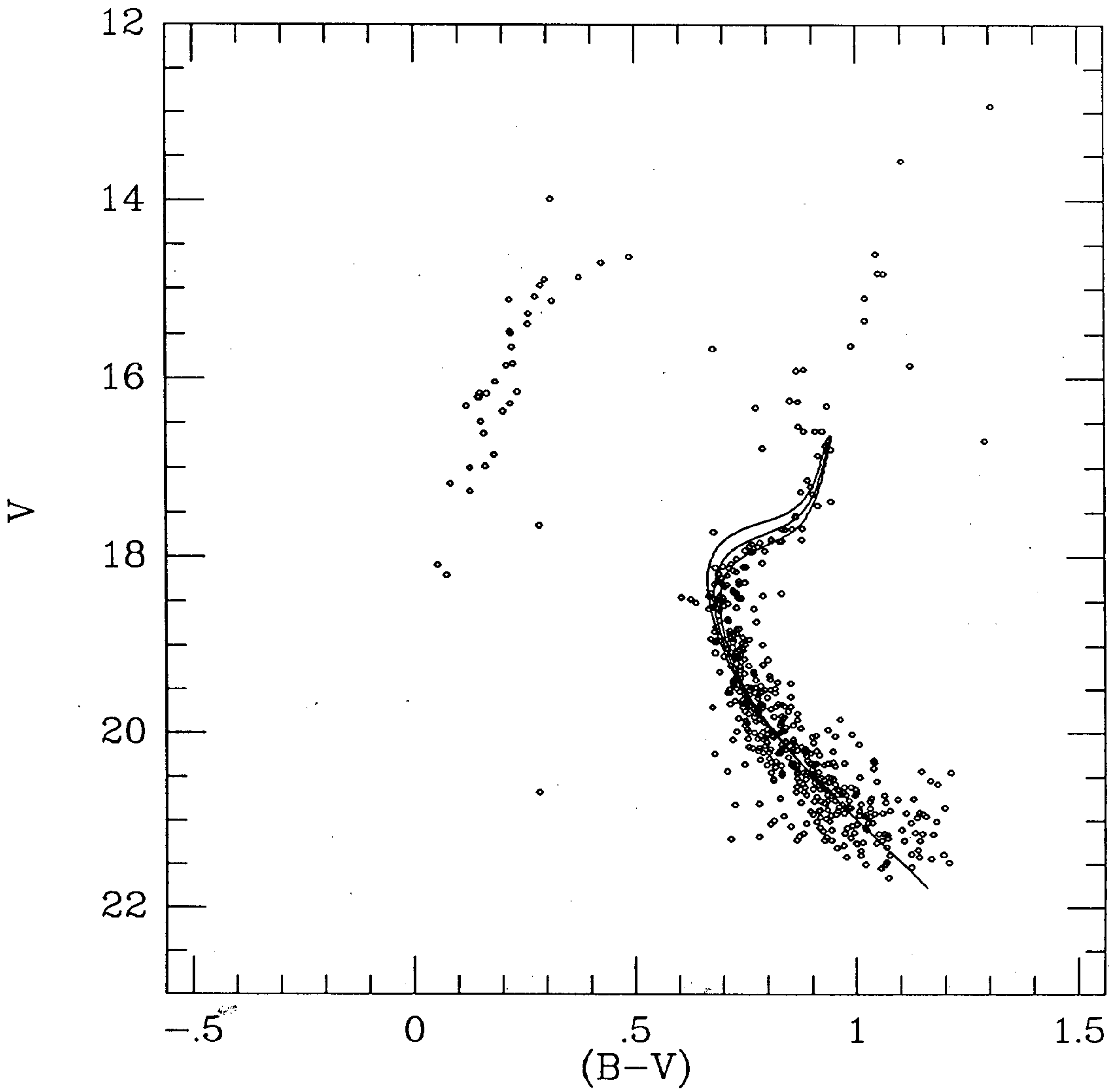

Figure 5.12: Isochrones for [Fe/H] = −1.54 overlaid on the M10 color-magnitude diagram. Isochrones are shifted by $(\mathrm{m}-\mathrm{M})_V = 14.4$ and $\mathrm{E}(B-V) = 0.273$. From left to right the isochrones are for ages 14,16,18 Gyr. A redward shift of 0.04 in color has been applied to the isochrones in addition to the reddening.

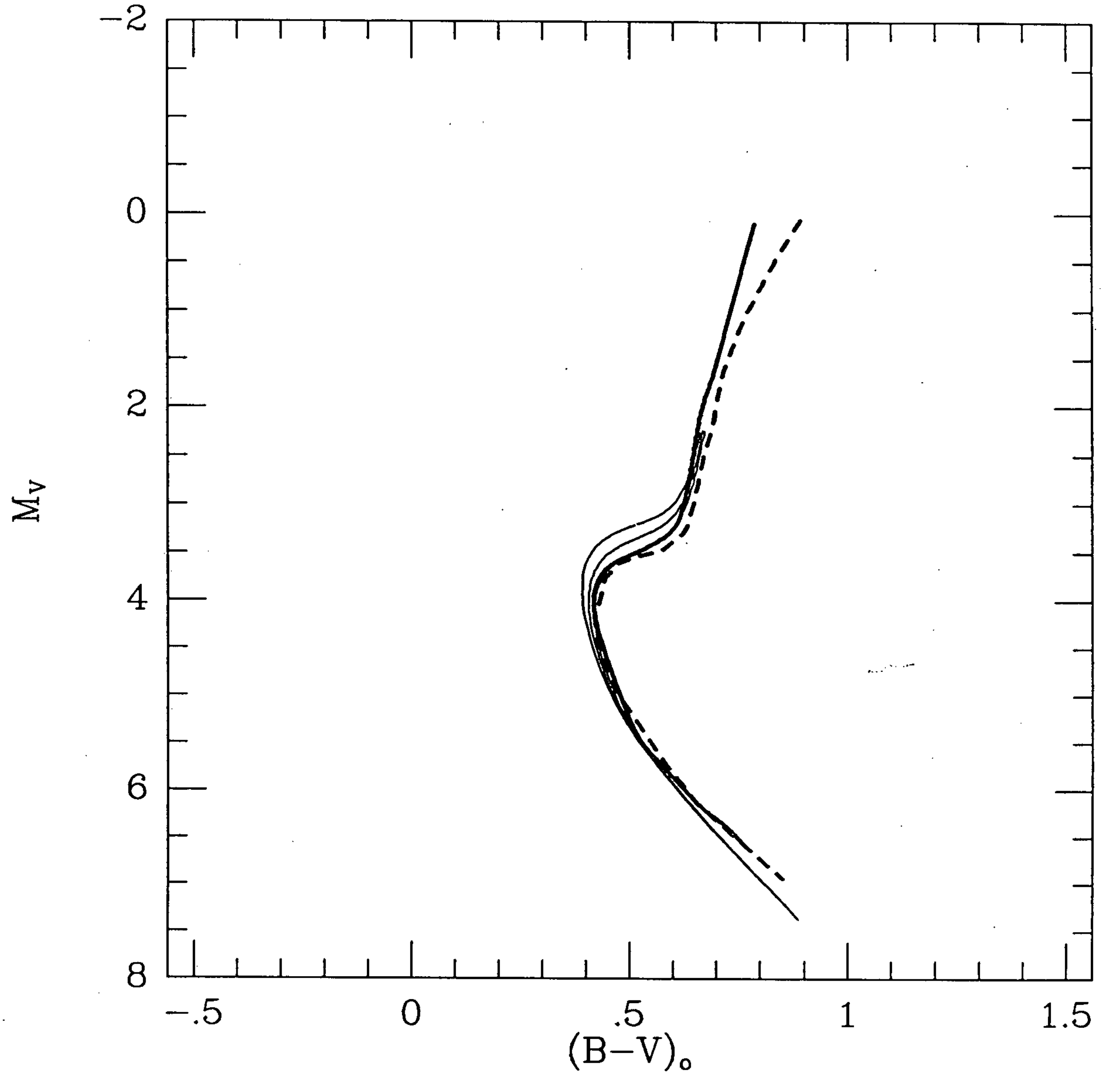

Figure 5.13: M10 and NGC 288 fiducials. The NGC 288 data (dashed) is from Bolte (1989b). The Isochrones are the same as those appearing in Figure 5.12.

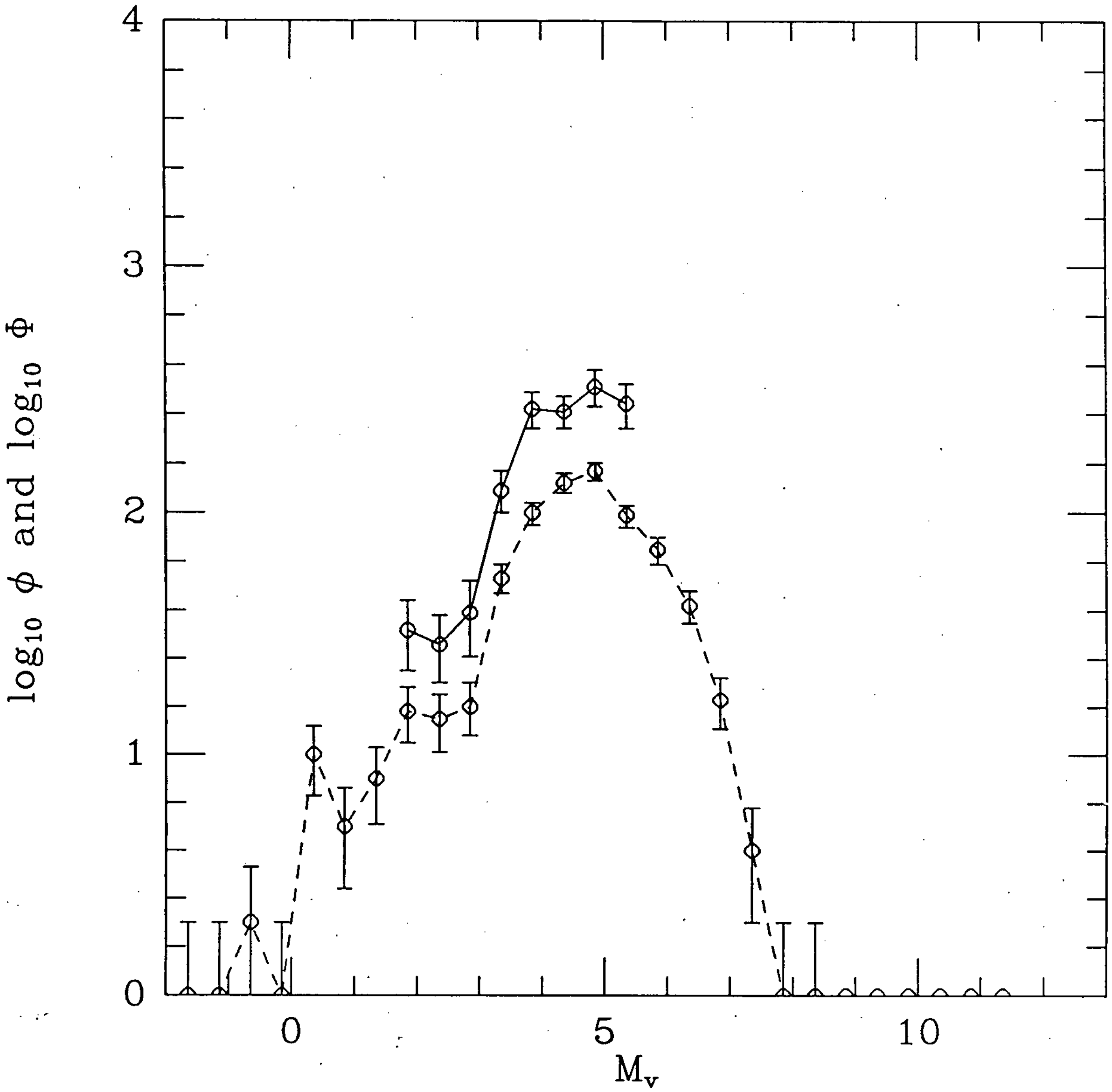

Figure 5.14: Inner Field luminosity function. The dashed line is the observed distribution of stars, ϕ. The solid line is the derived distribution, Φ.

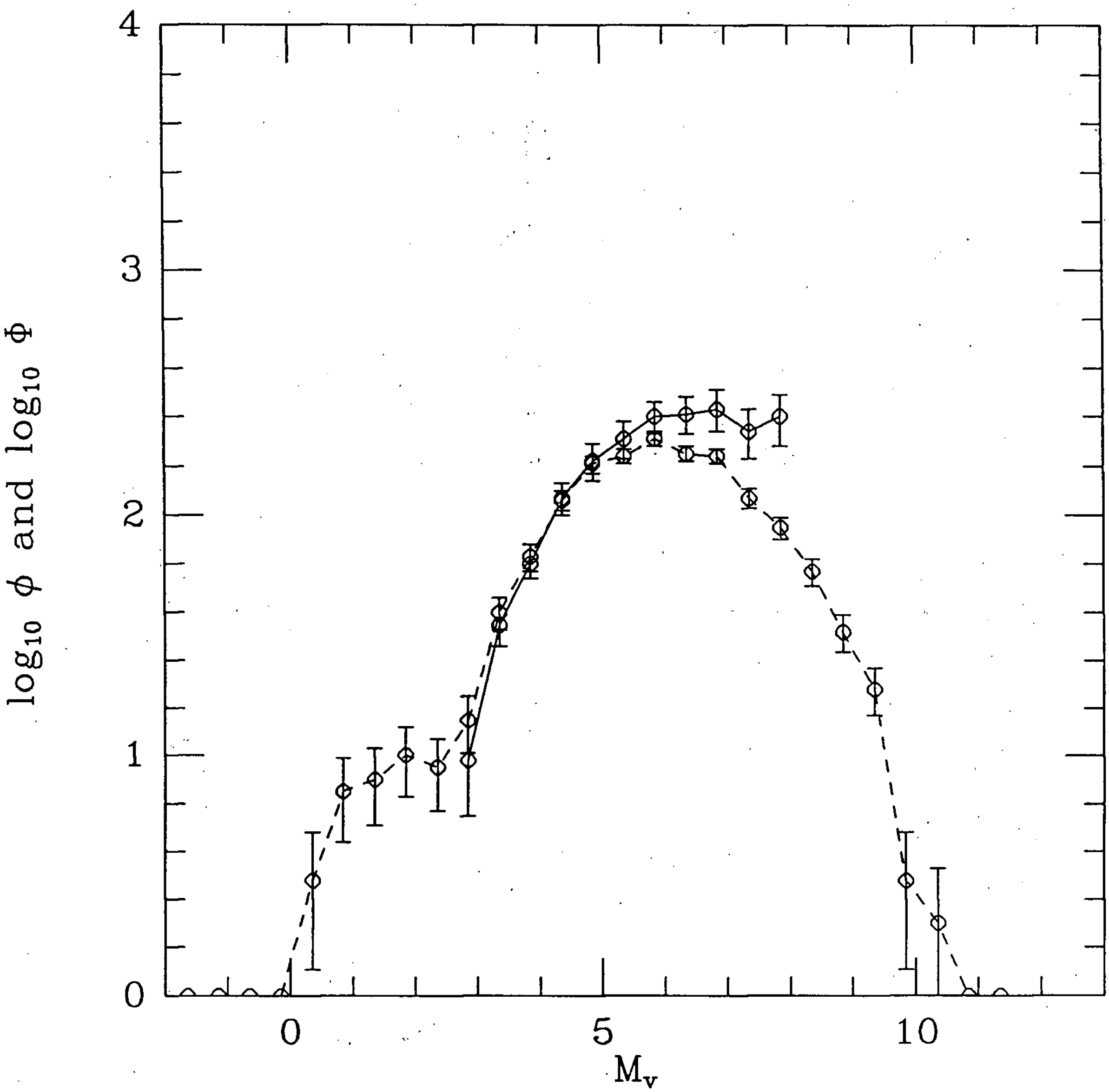

Figure 5.15: RCA2 Inner Field luminosity function. The dashed line is the observed distribution of stars, ϕ. The solid line is the derived distribution, Φ. Note that Φ may fall below ϕ due to field star corrections.

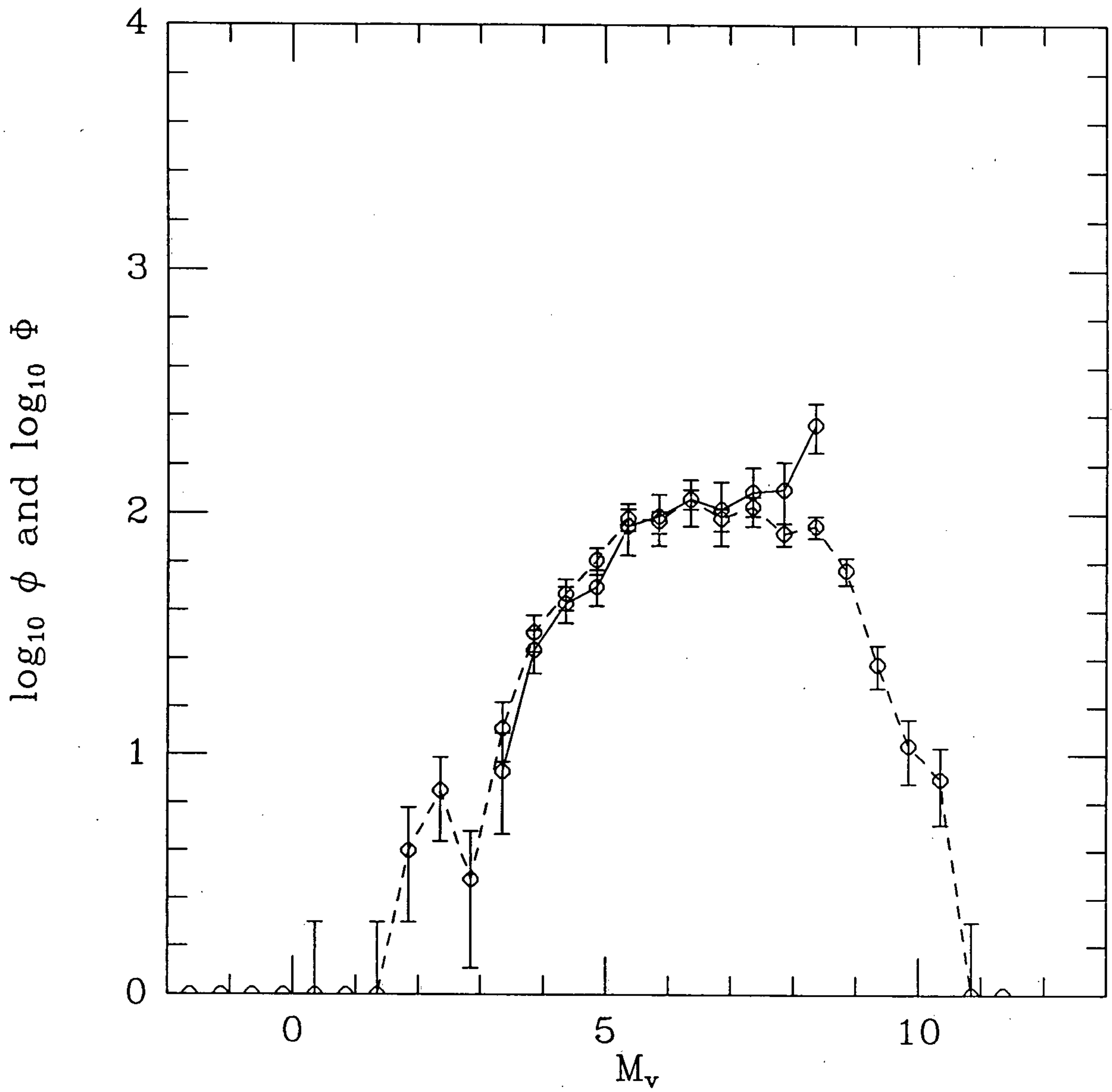

Figure 5.16: RCA2 Outer Field luminosity function. The dashed line is the observed distribution of stars, ϕ. The solid line is the derived distribution, Φ. Note that Φ may fall below ϕ due to field star corrections.

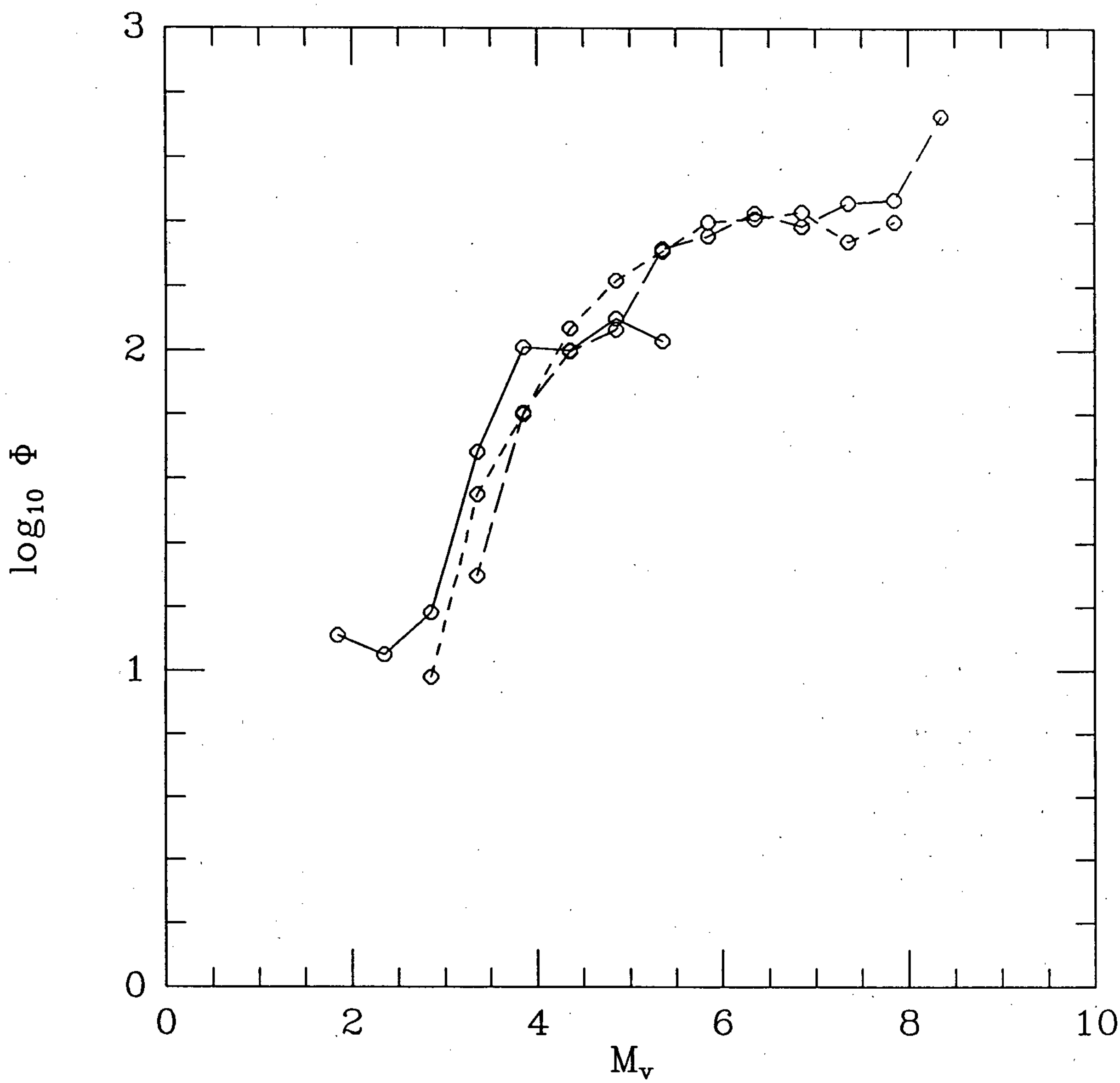

Figure 5.17: M10 luminosity functions. The solid line represents the Inner Field luminosity function. The long dashes represent the RCA2 Outer Field luminosity function. The short dashes represent the RCA2 Inner Field luminosity function. The Inner Field luminosity function is scaled to contain the same number of stars as the RCA2 Inner Field luminosity function between $M_V = 2.5$ and 5.0. The RCA2 Outer Field luminosity function is scaled to contain the same number of stars as the RCA2 Inner Field luminosity function between $M_V = 3.0$ and 8.0. The error bars have been omitted for clarity.

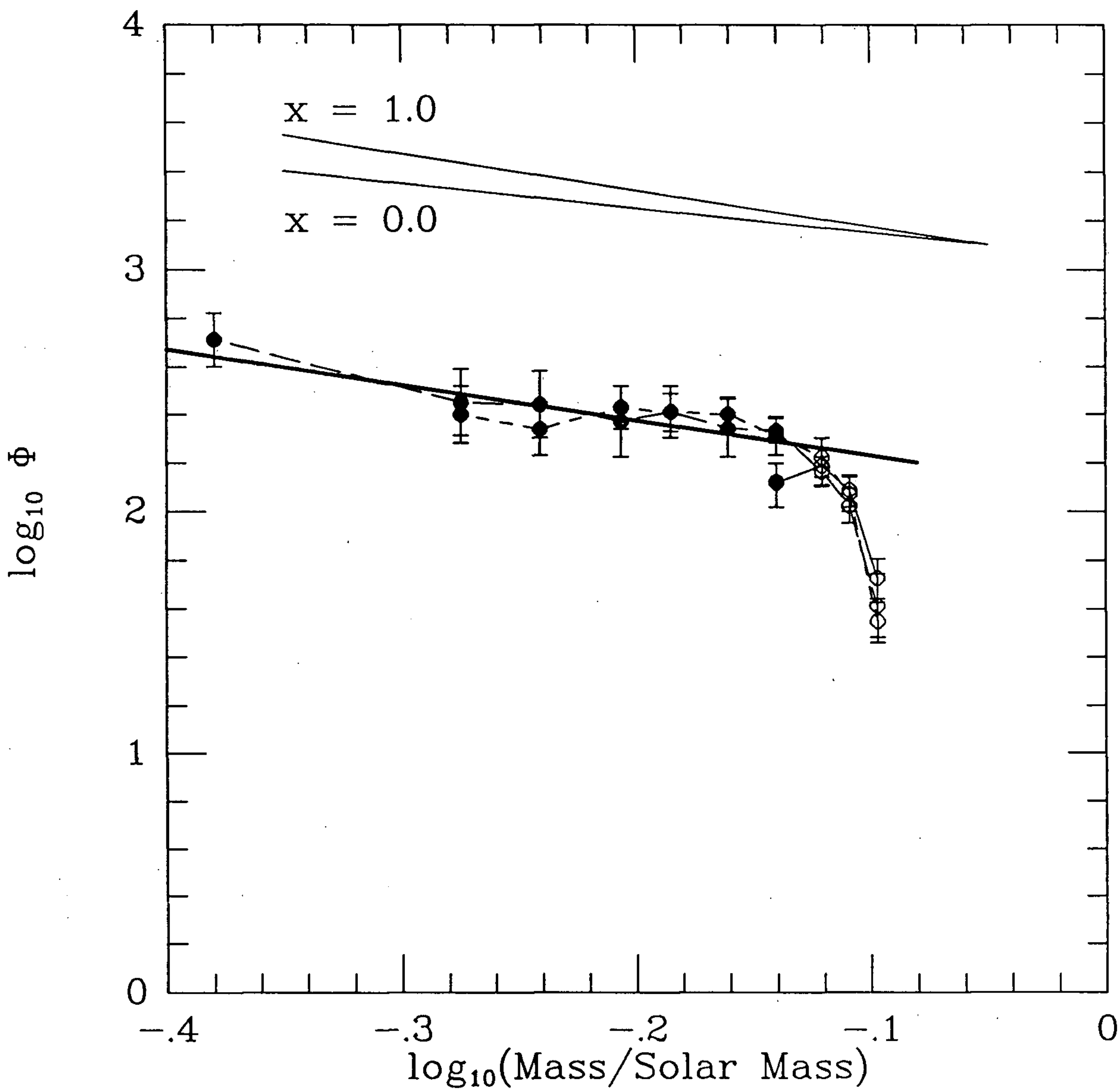

Figure 5.18: Mass functions. The solid line represents the Inner Field mass function. The long dashes represent the RCA2 Outer Field mass function. The short dashes represent the RCA2 Inner Field mass function. The bold line is a best least squares fit to the solid points, and corresponds to a mass function index of $x_{app} = 0.47$. The two lines at the top of the plot correspond to $x_{app} = 0.0$ and $x_{app} = 1.0$

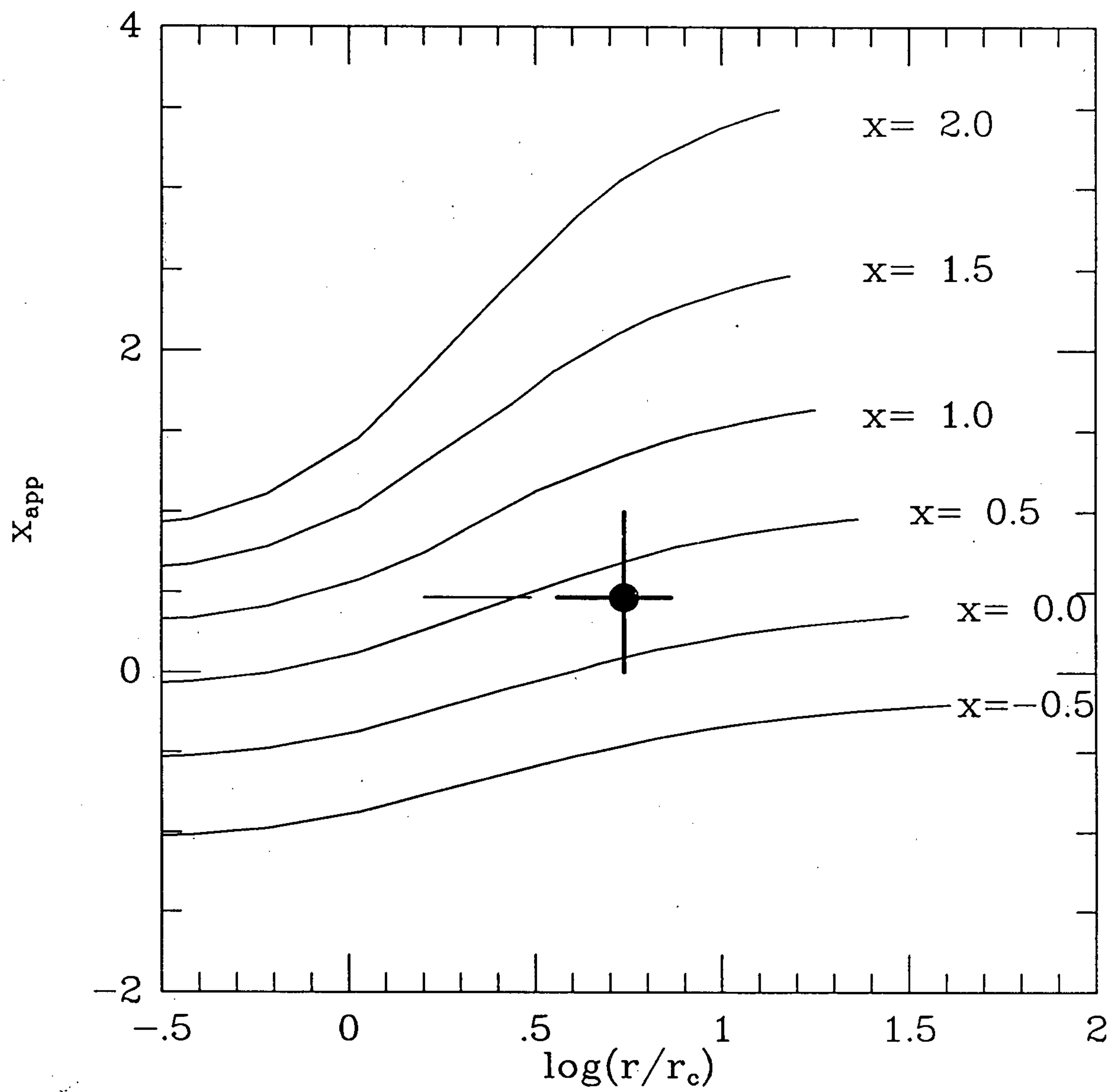

Figure 5.19: Global mass function exponent for M10. The curves represent multimass King models with different global mass function exponents. The vertical error bar is an estimate of the error in determining the local mass function exponent. The thick horizontal error bar spans the RCA2 Outer and RCA2 Inner Field, and the thin horizontal bar spans the Inner Field. The plotted point is placed midway between the RCA2 Inner and Outer Fields as these data most strongly influence the estimate of x_{app}.

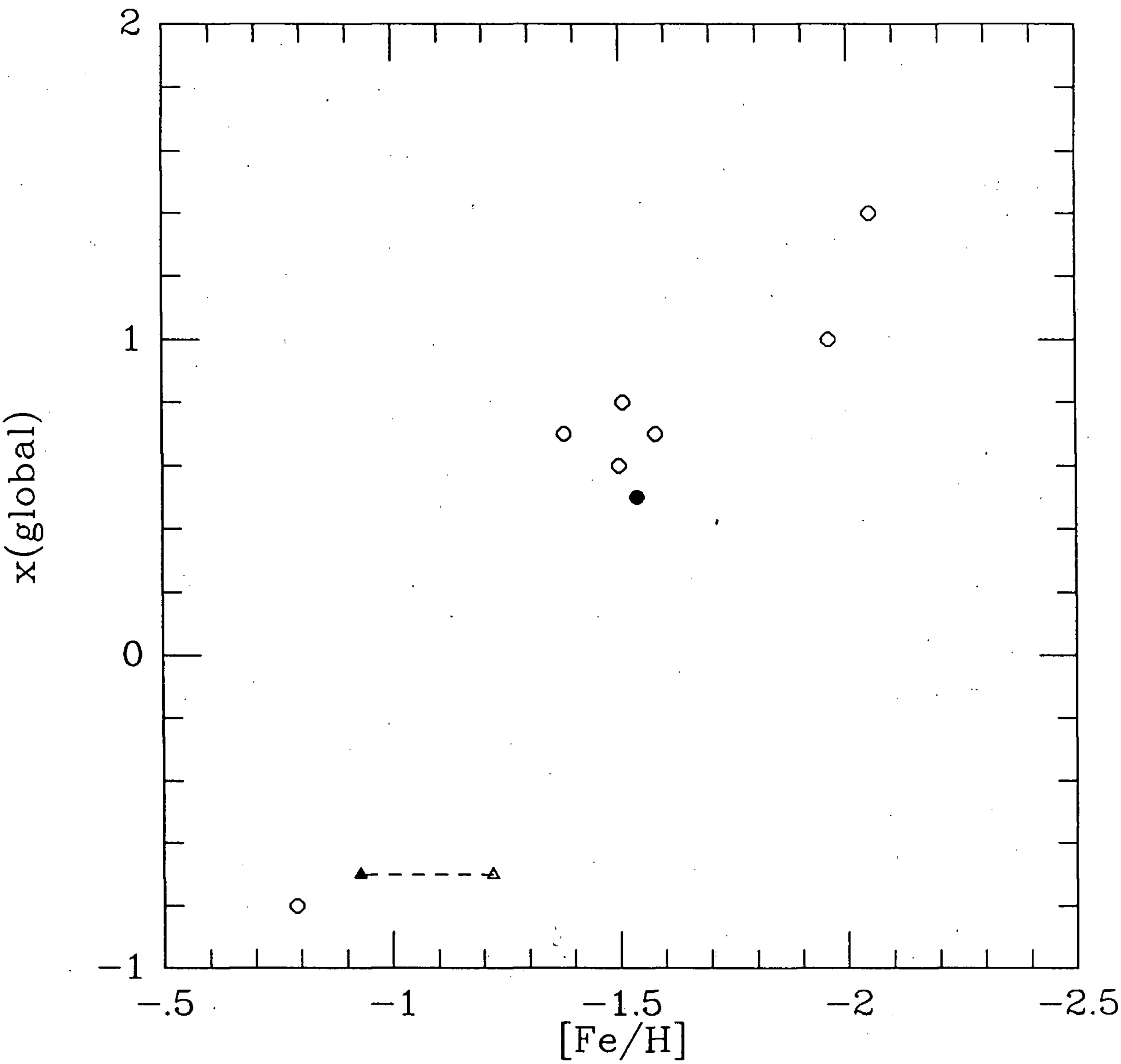

Figure 5.20: Metallicity versus global mass function exponent relationship. Open circles represent data from Pryor, Smith and McClure (1986). The solid circle represents M10. The open triangle represents the values reported in Pryor, Smith and McClure (1986) for M4. The solid triangle represents M4 with the same value for x_{global}, but with [Fe/H] $= -0.93$ as reported by Richer and Fahlman (1984). This brings M4 into much better agreement with the overall trend of the data.

Chapter 6

Conclusions

A deep color magnitude diagram for M10 has been produced. This diagram includes stars at brightnesses well below the main sequence turnoff, and a very blue horizontal branch which extends to at least the turnoff luminosity. These new data are well suited to determination of many cluster parameters.

The blue horizontal branch stars provide an estimate of the reddening $E(B-V) = 0.273 \pm 0.034$. The lower main sequence was compared to a fiducial of field subdwarfs to obtain a distance modulus $(m-M)_V = 14.4 \pm 0.2$. This value is higher than previous estimates. HRdR made two determinations of $(m-M)_V$ for M10, based on the level of the horizontal branch (assuming $M_V(HB) = 0^m.6$), and a comparison of the color-magnitude diagrams of M10 and M13. Both methods yielded distance moduli near $14^m.1$ These estimates are handicapped by the sparseness of the horizontal branch in the region of the RR Lyrae gap, as discussed in §5.2.1. Comparison of the new data to the photographic photometry of HRdR reveals a possible systematic difference of $\sim 0^m.2$ in V. This would raise the HRdR distance modulus to $14^m.3$, consistent with the value derived here to within the error limits.

From measurements of $\delta(U-B)$ on a $(B-V)$ versus $(U-B)$ color-color diagram a metallicity of $[Fe/H] = -1.54 \pm 0.4$ is found. The method employed in this work to determine [Fe/H] relies on a rather weak correlation, particularly in the region of intermediate metallicity, as seen in Figure 5.10. It is interesting to speculate that the dispersion in $\delta(U-B)_{0.6}$ at intermediate metallicites may be due to a second parameter. Two of the four intermediate metallicity clusters used in Figure 5.10 (M5 and M13) have very different horizontal branch morphologies, but very similar $\delta(U-B)_{0.6}$. This suggests that the dispersion in $\delta(U-B)_{0.6}$ does not depend upon horizontal branch morphology. Further work to strengthen the $\delta(U-B)_{0.6}$-metallicity correlation is called for. If the estimate of [Fe/H] were increased slightly it would agree better with the bluer horizontal branch population clusters in the correlation. However, there is no *a priori* reason to change the current estimate, which is in keeping with accepted values.

The age of M10 is estimated to be 17 ± 1 Gyr, from fitting to VandenBerg and Bell's (1985) theoretical isochrones. Comparison of this work to that of Bolte (1989b) shows that M10 is coeval with NGC 288 to within 2 Gyr. Like M10, NGC 288 also displays a larger than normal value of ΔV_{HB}^{TO}, an age sensitive parameter. Both these clusters contain exceptionally blue hroizontal branches for their metallicities, making them examples of second parameter clusters. Since both clusters are coeval and old (Bolte 1989b) the second parameter may be age.

Luminosity functions were prepared for M10 and converted to mass functions. Only a weak indication of mass segregation was observed; however, the observations are fairly insensitive to variations in the mass function exponent. The mass functions are quite constant in slope from $0.8M_\odot$ down to $0.5M_\odot$. The apparent mass function exponent was found to be $x_{app} = 0.5 \pm 0.5$ at $5r_c$. The corresponding global mass function exponent was found to be $x_{global} = 0.5 \pm 0.5$ using multi-mass King models. This value of global mass function exponent agrees well with the correlation between [Fe/H] and x_{global} noted by Pryor *et al.* (1986).

References

Arp, H. C. 1955, *A. J.*, **60**, 317.

Arp, H.C. 1962, *Ap. J.*, **135**, 311.

Arp, H.C. 1965, in *Galactic Structure*, ed. A. Blaauw and M. Schmidt (Chicago: University of Chicago Press), p.401.

Arp, H.C., and Hartwick, F.D.A. 1971, *Ap. J.*, **167**, 499.

Baade, W. 1944a, *Ap. J.*, **100**, 137.

Baade, W. 1944b, *Ap. J.*, **100**, 147.

Bolte, M. 1989a, preprint.

Bolte, M. 1989b, preprint.

Buonanno, R., Corsi, C.E., Fusi Pecci, F. 1988, preprint.

Canada-France-Hawaii Telescope Corporation, Observers Manual, third edition, 1988.

Carney, B.W. 1979, *A.J.*, **84**, 515.

Chandrasekhar, S. 1943a, *Rev. Mod. Phys.*, **15**, 1.

Chandrasekhar, S. 1943b, *Ap. J.*, **98**, 54.

Chandrasekhar, S. 1960, *Principles of Stellar Dyanamics*, (New York: Dover).

Drukier, G. A., Fahlman, G.G., Richer, H.B., VandenBerg, D.A. 1988, *Ap. J.*, **95**, 1415.

Fahlman, G.G., Richer, H.B., VandenBerg, D.A. 1985, *Ap. J. Supp.*, **58**, 225.

Gratton, R.G. and Ortolani, S. 1988, *Astr. Astrophys. Suppl.*, **73**,137.

Gunn, J. E., and Griffin, R. F. 1979, *Astron. J.*, **84**, 752.

Harris, W. E., and Racine, R. 1979, *Ann. Rev. Astron. Astrophys*, **17** , 241.

Harris, W. E., Racine, R., deRoux, J. 1976, *Ap. J. Supp.*, **31**, 13 (HRdR).

Hesser, J.E., and Hartwick, F.D.A. 1977, *Ap. J. Supp.*, **33**, 361.

Hesser, J.E., *et. al.* 1987, *P.A.S.P.*, **99**, 739.

King, I. R. 1966a, *Astron. J.*, **71**, 64.

King, I. R. 1966b, *Astron. J.*, **71**, 276.

Kron, G. E., Hewitt, A. V., Wasserman, L. H. 1984, *P.A.S.P.*, **96**, 198.

Landolt, A. U. 1973, *A.J.*, **78**, 959.

Landolt, A. U. 1983, *A.J.*, **88**, 439.

Lightman, A. P., and Shapiro, S. L. 1978, *Rev. Mod. Phys*, **50**, 437.

Lynden-Bell, D., 1967, *M. N. R. A. S.*, **136**, 101.

Lutz, T.E., Hanson, R. B., van Altena, W.F., 1987, private communication.

Mihalas, D., and Binney, J, 1981, *Galactic Astronomy, second edition*, (San Fransisco: Freeman).

Nemec, J.M. 1978, M.Sc. thesis. University of Victoria.

Osborn, W. 1973, *Ap. J.*, **186**, 725.

Pound, M.W., Janes, K.A., Heasley, J.N. 1987, *A. J.*,**94**, 1185.

Peterson, C. J., and King, I. R. 1975, *Astron. J.*, **80**, 427.

Pryor, C., Smith, G. H., McClure, R.D. 1986, *A. J.*, **92**, 1358.

Ratnatunga, K.U., and Bachall, J.N. 1985, *Ap.J.*, **59**, 63.

Richer, H.B., and Fahlman, G.G. 1984, *Ap. J.*, **277**, 227.

Richer, H.B., and Fahlman, G.G. 1986, *Ap. J.*, **304**, 273.

Richer, H.B., and Fahlman, G.G. 1987, *Ap. J.*, **316**, 189.

Samus', N. N., and Shugarov, S. Yu. 1983, *Sov. Astron.*, **27**(6), 1091.

Sandage, A. 1969, *Ap. J.*, **158**, **1115**.

Sandage, A. 1970, *Ap. J.*, **162**, 841.

Sawyer Hogg, H. 1973, *David Dunlap Pub.*, *Vol. 3*, No. 6.

Shapley, H. 1918, *Ap. J.*, **48**, 89.

Spitzer L. 1984, *Science*, **225**, 465.

Spitzer, L. 1987, *Dynamical Evolution of Globular Clusters*, (Princton: Princeton University Press).

Stetson, P. B. 1987, *P.A.S.P.*, **99**, 191.

Stetson, P.B., and Harris, W.E. 1988, *A. J.*, **96**, 909.

VandenBerg, D.A., and Bell, R.A. 1985, *Ap. J. Supp.*, **58**, 561.

Webbink, R. F. 1985, in *IAU Symposium 113, Dyanamics of Star Clusters*, ed. J. Goodman and P. Hut (Dordrecht: Reidel), p. 541.

Zinn, R.J. 1980, *Ap. J.*, **241**, 602.

Zinn, R.J., West, M.J. 1984, *Ap. J. Supp.*, **55**, 45.

Zinn, R.J. 1986, in *Stellar Populations*, ed. C.A. Norman, A. Renzini, and M. Tosi (Cambridge: Cambridge University Press), p.73.